

Fibration symmetries and cluster synchronization in the *Caenorhabditis elegans* connectome

Bryant Avila¹, Matteo Serafino¹, Pedro Augusto^{2,4}, Manuel Zimmer^{3,4},
Hernán A. Makse^{1*}

1 Levich Institute and Physics Department, City College of New York, New York, NY 10031, USA

2 Vienna Biocenter PhD Program, Doctoral School of the University of Vienna and Medical University of Vienna, 1030, Vienna, Austria

3 Research Institute of Molecular Pathology (IMP), Vienna Biocenter (VBC), Campus-Vienna-Biocenter 1, 1030 Vienna, Austria

4 Department of Neuroscience and Developmental Biology, Vienna Biocenter (VBC), University of Vienna, Djerassiplatz 1, 1030 Vienna, Austria

* hmakse@ccny.cuny.edu

Abstract

Capturing how the *Caenorhabditis elegans* connectome structure gives rise to its neuron functionality remains unclear. It is through fiber symmetries found in its neuronal connectivity that synchronization of a group of neurons can be determined. To understand these we investigate graph symmetries and search for such in the symmetrized versions of the forward and backward locomotive sub-networks of the *Caenorhabditis elegans* worm neuron network. The use of ordinary differential equations simulations admissible to these graphs are used to validate the predictions of these fiber symmetries and are compared to the more restrictive orbit symmetries. Additionally fibration symmetries are used to decompose these graphs into their fundamental building blocks which reveal units formed by nested loops or multilayered fibers. It is found that fiber symmetries of the connectome can accurately predict neuronal synchronization even under not idealized connectivity as long as the dynamics are within stable regimes of simulations.

Introduction

Advances in reconstructing synapse resolution wiring diagrams of various model organisms [1–6], demand the development of new computational tools that make predictions of how neuronal wiring relates to neuronal function [7]. The nematode *C. elegans* is an ideal system to prototype such approaches because of its fully mapped and well characterized small nervous system of just 302 neurons [1, 8–10]. Various studies have identified structure in the wiring architecture of the worm connectome e.g., over-represented network motifs [8, 11], small worldness [12], rich club topology [13] as well as community structure and functional layers [9, 14–16]. While such features suggest functional implications such as sensory-motor flow or wiring economy, they typically fall short of making concrete predictions for how neurons dynamically interact with each other.

One notable type of dynamics observed in *C. elegans* is the brain-wide synchronization of neural activity across well-defined ensemble of neurons ; where a

general notion of synchronization is that larger ensembles of neurons have correlated activity patterns [17–19]. Understanding how such synchronizations are supported by the underlying connectome is a major challenge in neuroscience and can provide mechanistic insights into how the brain processes information. We recently showed that primary and secondary input similarities predict pairwise synchronizations in *C. elegans* neuronal dynamics [17] hinting at symmetries in the larger network context underlying such synchronisations. A mathematically precise description of such input similarities was missing with which symmetries could be uncovered. Therefore, it is important to better define the structures in the connectome that lead to the synchronization of groups of neurons [20, 21] based on their inputs.

Synchronization is ubiquitous across all organisms and at different scales. Some examples are gene co-expression patterns [22], metabolism, hormonal regulation, cell communication, and cardiac muscle. As such, the results on this direction may be generalized to the different levels of synchronization in biological networks.

From a theoretical perspective, it is well known that the symmetries of the underlying network, including automorphisms (orbits) [23–25] and fibrations (fibers) [26–30], can strongly determine the dynamics of the system leading to synchronization of neurons within clusters [31–33], i.e. cluster synchronization. Orbits are related to particular permutations (automorphism) of the network that preserve the network’s adjacency connectivity structure- including both in-degree and out-degree. The cluster of nodes subject to these permutations are called orbits, and nodes in orbits synchronize their activity under a suitable dynamical system that is admissible with the network [23, 29, 33]. Where this synchronization is accomplished when two or more neurons share a set of neurons as their inputs and where these inputs have equivalent connectivity structures; such synchronization is explained further in the paper.

The requirements for the existence of orbits are strict, as they must preserve the entire adjacency matrix network structure. Synchronization of neuronal activity patterns, on the other hand, only requires constraints on the nodes’ inputs (in-degree), not the outputs (out-degree).

Fibrations are symmetries that generate automorphisms only requiring the invariance of the input tree structure of each node [27, 28, 32, 34–36]. These symmetries form symmetry groupoids rather than symmetry groups of automorphisms where these define fibers similarly to orbits, where nodes in the same fiber synchronize [37]. In this sense, a groupoid is a more general algebraic structure than a group, where a groupoid need not be associative; by such fibers are more general than orbits, as they are related to equivalent classes which are referred to in the math community as *balanced coloring*. Every orbit is a fiber, but not every fiber is an orbit. Therefore fibers capture more patterns of cluster synchronization than orbits. Therefore, we here propose that fibers are a more general and mathematical defined description of connectivity that relate to the input similarities investigated in ref. [17]. In [37] we have found automorphisms in the structure of the *C. elegans* connectome, specifically in the gap junction and chemical synapses networks of motor circuits involved in forward and backward locomotion. Here we generalize this study to search for more general patterns of symmetry fibrations and their associated fibers of cluster synchronization in the *C. elegans* locomotive connectome.

Given their mild constraints, biological networks tend to have more fibers than orbits. In [26], we have found that gene regulatory networks of many organisms spanning from simple bacteria to humans are composed of fibration symmetries. These symmetries partition the network into synchronized fibers which are then the building units characterizing the structure of such networks. As such, fibrations can be thought of as the ”building blocks” of a network, in the sense that they represent the

fundamental units or components that can be combined to form larger and more complex structures or systems. According to [38], the building blocks of a network can be thought of as the "units of computation" in a neural network, similar to how transistors constitute the basic building blocks of electronic circuits.

The concept of building blocks as a way to modularly construct neural networks with specific desired properties is familiar in the field. In [39–41] a framework has been proposed for understanding the function and organization of neural networks in terms of building blocks known as "network motifs." Network motifs are small, recurring patterns of connections within a network that are thought to perform specific functions or play a role in shaping the network's overall structure and function.

Symmetries in the connectome can only tell us about the existence of synchronized solutions but not about the stability of such solutions. If a group of neurons were prepared to be in a synchronous state, theory predicts that these will stay in such a state indefinitely if no noise is present [25, 42]. However, if the system were to start in any other initial condition, would it evolve towards a synchronized state, such as a fixed point? If so, the synchronous state is considered to be stable. If not, the synchronous state is considered to be unstable, such that most, if not all, neurons have different values at any given time (asynchronous). The structure of the connectome alone cannot predict their stability. Stability also depends on the particular system of equations that define the neural dynamics of the system. It is not a property that is inherent to the fibration symmetry itself but rather a property that emerges from the interactions between fibers and their surroundings through the dynamical system. Thus, a single symmetric connectome leads to synchronous solutions, but these solutions could have different stability properties according to different dynamical systems of equations. Since the same connectome with a different dynamic system may lead to a stable or unstable solution, stability needs to be investigated for each particular dynamical system of equations [25, 42].

In this paper, we explore the structure-function relationship of a version of the neuron network in *C. elegans* used in [26] related to the locomotion function (as described later) to characterize its fibration symmetries and its comparison with automorphisms. Generalizing the results found in [37] on the existence of automorphisms, here we further studied the more general fibrations, their associated fiber partitions, and their relations with the orbital partitions obtained from automorphisms. We apply a set of simplifications to make our theoretical and modeling approaches tractable and which are prerequisite to identify the orbits and fibers in this study in a mathematically concise manner. First, we focus on sub-networks that have been assigned to distinct behavioral functions of *C. elegans*. Next, we study the graphs of chemical synapse and gap junction networks in isolation. Moreover, we apply subtle modifications (repairs) since the mathematical procedures applied here are strict and do not account for variability in connectome data and even slight deviations from perfect symmetries. Lastly, we use simplified neuronal models that treat each network node as if they had identical dynamical properties. These models solely serve as a test case to confirm that our predictions about cluster synchronizations hold in the context of a dynamical system, in contrast to a sole static neuronal connectome. Below, we will discuss the implications of our findings, made under these simplifications, for the worms neuronal network functions and behaviors it produces. We compare the synchronous solutions obtained from a dynamical system of interacting neuron equations with the ones predicted by the fibers of the connectome and investigate their stability under different initial conditions. Simulating the dynamics of neurons is achieved by mapping admissible in-degree dependent coupled ordinary differential equations (ODEs), as explained further in the paper. We characterize the locomotion connectome into fiber building blocks organized into classes according to some of their structural properties,

such as, how many inputs these have and a characterization of how many closed paths these inputs form with the fiber. These building blocks are similar to those found in genetic networks [26] implying the generality of these blocks for the structure of biological networks.

We follow two steps. First, we partition the neuron network using fibrations and automorphisms. As anticipated, we find that biological networks tend to have more fibers than orbits when examining a directed network of chemical synapses. In the network of gap junctions, the fibers are the same as the orbits as expected for an undirected network. Next, we investigate the stability of the synchronous solutions predicted by the symmetries when the network is exposed to different external stimuli using ordinary differential equations (ODEs). Initially, we observe that without an external driving force the ODEs settle into the same synchronization groups as predicted by symmetries and expected by theory. Then we examine the synchronizations that occur in the network when it is driven by an external driving input; its observed that these stimulated neurons react in a stable fashion similarly like a set of neurons in electrophysiological studies when stimulated with an external current source [43, 44]. We find that instabilities can appear above certain magnitudes for the external input which are model dependent. We then simulate the case where the network's weight edges are not fully known and study the impact of this missing information on the synchronization states. We found that the effects of varying weights impact the synchronicities of the networks. The robustness to change varies among the different types of networks, with the Gap networks being more robust to change.

We conclude our analysis by focusing on the partition of fibers, which serve as building blocks for each of the networks studied here. These can be topologically categorized, information that in turn can be used to determine the relative stability against perturbations for each fiber. The symmetries structures and the synchrony patterns we find here could be tested in in-vivo in the future by opto-genetically silencing or ablating neurons which would affect the synchronization predicted by fibers. [45, 46]. Some building blocks with different structure can belong to the same topological classification where their functionality could be tested by analyzing the similarity of the dynamics of the neurons belonging to the same fiber.

The paper is structured as follows. The locomotion network section for the latter portion of the Introduction and focuses on the construction of the neurons' network and the data set used in this paper. Then in Fibers and orbits the theory used in this paper is introduced which covers equitable partitioning, fibers, orbits and the methods used for our analysis, followed by the section Building blocks in which fibers are used to construct elementary sub-networks which form the locomotion network. Ending the theory presentation with Admissible ODEs that outlines the admissible ODEs used to conduct simulation tests and with Synchronicity measure. After the theory we move into the results with first showing in Network partitions in the locomotion connectome how the locomotion networks of the *C. elegans* are partitioned by fibers and orbits. Additionally the fiber building blocks of the directed networks are shown. Results are concluded in Network simulations with the synchronicities found from numerical methods solving ODEs applicable to the worm neuron system. Wrapping up with the sections of Discussion and conclusion Conclusion.

The locomotion network

A comprehensive analysis of orbits across the entire connectome is currently out of reach, due to computational constraints. Therefore, we focus on two locomotion sub-networks implicated in the generation of two distinct gaits: forward and backward behaviour. One major reason for this selection is the fact that the *C. elegans*

locomotion network has feedforward excitatory synapses from the command interneurons to their respective motor-neurons, inducing a highly synchronous state in all neurons which participate in the motor output. In addition, secRNA seq data has shown that motor-neurons represent the most similar class of neurons in the worm, which further supports the comparisons made later in this study [47]. The networks present in this paper are manually repaired version of the Varshney connectome (available at the WormAtlas website [48]). Such repaired networks have been validated by integer programming repair algorithms, one based on full fibration analysis [49] and another on quasi-fibrations [35]. The former leads to the network solutions found in [37] and studied here when provided with a set of groups of neurons belonging to each fiber. The reason behind such repairs is to bring to the front the rich number of symmetries in the raw connectome with only a few modification to it. Where without modification each neuron exhibits its own unique symmetry, the slightly modified connectome captures multiple groups neurons belonging to one symmetry. The repairs were done by hand by removing and adding a minimum amount of edges which would reduce the number of fibrations in each graph by the largest amount possible given the restriction that the each change of the network was not outside natural variation of edges of 25% [8, 37], where most modification did not reach the 25% variation. The repairs allow us to focus on the neurons with evidence to be involved exclusively in this animal's forward or backward locomotion. It includes inter-neurons AVB, PVC, and RIB for the forward system, inter-neurons AIB, AVA, AVD, AVE, and RIM for the backward system [50–52] and four classes of motor-neurons: DA, VA for the forward system and DB, VB for the backward system [53]. The remaining motor neurons (AS, DD, and VD) have not been included in the studied networks. This strategy is based on previous experimental findings showing that AS neurons are not mutually exclusively involved in either forward or backward movement [54]; inhibitory GABAergic DD and VD motor neurons are not strictly required for movement, i.e. when removed or blocked, the animal moves indistinguishably at a lower frequency and does not produce higher-frequency undulations. Nevertheless, it does not eliminate the ability to move forward, or backward [55]. The exclusion of DD and VD motor neurons allows partitioning the neurons mentioned above into two not overlapping functional sets (forward and backward locomotion). This stratagem avoids neurons belonging to multiple synchronization modes, resulting in more interpretable results.

Neurons in *C. elegans* can be physically connected through chemical synapses or gap junctions. Chemical synapses are directed connections meaning that a chemical signal can only propagate in one direction (from neuron A to neuron B and not vice versa) [56]. Gap junctions, on the other hand, can lead to undirected connections, allowing rapid propagation of an electrical signal between two connected neurons in both directions [57]. Henceforth, we apply this simplification and ignore the possibility of rectifying gap junctions [58]. As such, the neuron network in the *C. elegans* can be represented by two adjacency matrices, one for each type of connection, chemical synapses and gap junctions. To better comprehend these two types of connections and their co-occurrence, we redirect the reader to [8].

Removing the inter-connections between the two functional sets of neurons for the forward and backward locomotion leads to four independent adjacency matrices representing the *C. elegans* locomotion system [37]: Forward gap junction (F-Gap), backward gap junction (B-Gap), forward chemical synapses (F-Chem), and backward chemical synapses (B-Chem) networks. Note, that this partitioning into forward and backward groups is justified since activity of these sub-networks has been shown to be mutually exclusive and tightly associated with either one of the two distinct motor programs [59–61]. In the original work of [37], the networks and their respective adjacency matrices are binary, meaning the connections between neurons either have a

weight of 1 for existing edges or 0 for non-existing edges. In this paper, we also introduce and analyze the integer-weighted version of these sub-networks, where weights have positive integer values reflecting the number of synaptic connections between neurons based on Varshney’s connectome [8]. These weights respect the symmetrization done by [37] and the fiber partitionings corresponding to the binary versions. This leads to a total of 4 sub-networks each with two edge weight versions under study.

Materials and Methods

Fibers and orbits

The neural networks governing the movement of *C. elegans* are represented as a graph $G = (N_G, E_G)$, where N_G is the set of nodes (neurons) with $n = |N_G|$ being the number of nodes and E_G is the set of connections among neurons. Chemical synapse networks consist of directed connections denoted as $e_G^{u \rightarrow v}$ from neuron u to neuron v , while gap junction networks consist of undirected connections $e_G^{u \leftrightarrow v}$ between neurons u and v . A general connection in E_G would simply be denoted as e_G . A connection is represented as ordered pairs of nodes for directed connections (u, v) , where v is the head node and u is the tail node. We interchangeably refer to these two types of connections as edges through out the paper. For undirected connections, two directed connections in opposite directions are used. Each edge has a head node $h(e_G^{u \rightarrow v}) = v$ and a tail node $t(e_G^{u \rightarrow v}) = u$.

Partitioning methods detect clusters of nodes with shared properties in a network. Two standard methods for partitioning networks into synchronized groups of neurons are Fiber [26–30] and Orbit partitioning [23–25]. These methods partition the n nodes of a graph G into groups of nodes which synchronize under admissible ODE dynamics [30–32, 62]. Admissible ODEs ensure that each node in the network has one ODE which is coupled to other ODEs in the same way its representative node receives connections. If the initial states of the nodes are within the stable regime of their given set of ODEs, then the nodes belonging to each partition will eventually reach synchronicity [29, 63]. Before diving into these methods, we must introduce the concept of equitable partition.

Loosely speaking, partitioning the n nodes of a graph G into groups that are in-degree conserving is an ”equitable partitioning”; these groups of nodes are referred to as *cluster cells*. More precisely, a partition π of G with cells C_1, \dots, C_k is equitable if the number of in-degree edges from C_j onto a node $v \in C_i$ depends only on the choice of C_i and C_j . Neurons in the same cluster cell have the same *balanced coloring* [32]. The out-degree can also be considered, but the in-degree conservation alone is sufficient for synchronization, and is therefore used in this paper [24, 25]. Fiber and orbit partitioning are examples of balanced colored partitioning methods with distinct characteristics, which are explained below.

Fibrations and the minimal balanced coloring

A fiber partitioning relies on the notion of neighboring nodes. We begin by defining the immediate in-degree neighboring nodes of a given node v as the multi-set of nodes fulfilling the following condition

$$t(e_G^{1 \rightarrow v}) = [u : u \in N_G \wedge (u, v) \in E_G] \quad (1)$$

where the multi-set of edges connecting into node v are given by

$$e_G^{1 \rightarrow v} = [(e_G, 1) : e_G \in E_G \wedge h(e_G) = v] \quad (2)$$

where (e_G, i) is a pair given by a positive integer number i indicating the length of a path terminating in v and an edge at the start of said path.

Given the above the fiber partitioning is associated with the input history of a node, which includes the input edges it receives from its immediate neighboring nodes, as well as the input those nodes receive from their immediate neighboring nodes. This notion can be extended an infinite number of times, resulting in an infinite *input tree* [23]. The input tree for a node v is denoted as $\mathcal{T}(v)$, which is the complete set of all paths that terminate on node v , giving rise to a rooted tree graph [28]. Such a structure can be placed in mathematical terms as

$$\mathcal{T}(v) = \bigcup_{i=1}^{\infty} \bigcup_{m=t(e_G^{i \rightarrow v})} e_G^{i+1 \rightarrow m} = \bigcup_{i=1}^{\infty} \bigcup_{m=t(e_G^{i \rightarrow v})} [(e_G, i+1) : e_G \in E_G \wedge h(e_G) = m]. \quad (3)$$

An input tree can be represented visually, as shown in Fig 1, which illustrates the input history of nodes E and F in the network shown in Fig 2a. Each node in the network has its own input tree, which may appear different at first. However, if the labels of the nodes and edges are ignored, a symmetry can be uncovered, revealing that some nodes in the network have the same input tree structure. These structures are referred to as *isomorphic input trees*, which are bijective mappings from one input tree \mathcal{T} to another input tree \mathcal{U} , such that there is a one-to-one mapping of nodes and edges from the n th layer of tree \mathcal{T} to the n th layer of tree \mathcal{U} [64].

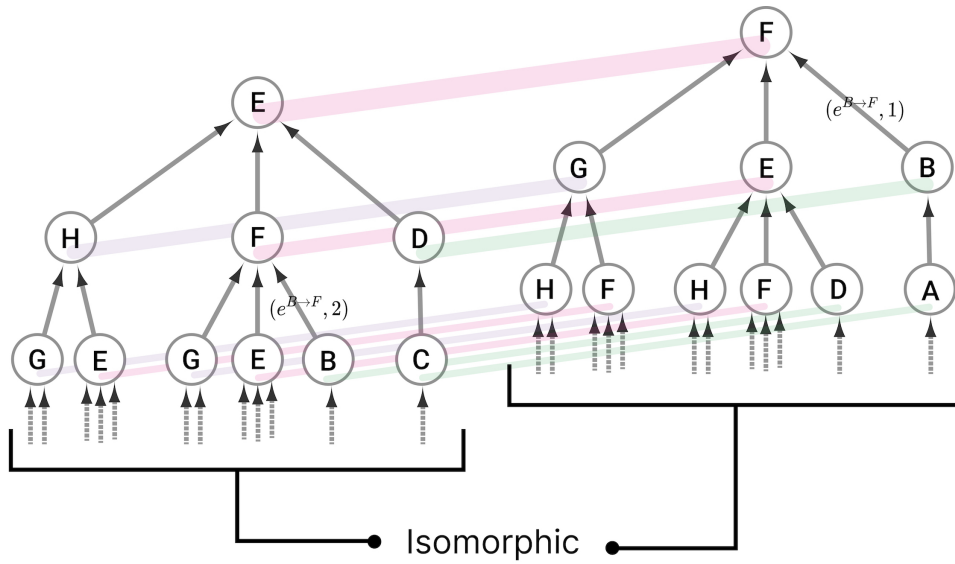


Fig 1. Input trees and their isomorphism. The input trees of nodes E and F for the network in Fig 2a are shown. The input tree of node E is given by all the possible paths in the network in Fig 2a which terminate on node E. All paths can be overlaid together forming a rooted tree graph which is referred to as the input tree. In this example only the first three layers of the input trees of nodes E and F are shown, but it can already be seen that their input trees are identical if all the labels of the nodes and edges are ignored. Nodes with isomorphic input trees eventually synchronize regardless of synaptic delay or small variations there parameters [65,66]. Colored lines indicate the morphism between trees. An input tree can be annotated by the number of edges between specific nodes at specified layers, the edge from B to F is shown for both input trees where it appears at different layers.

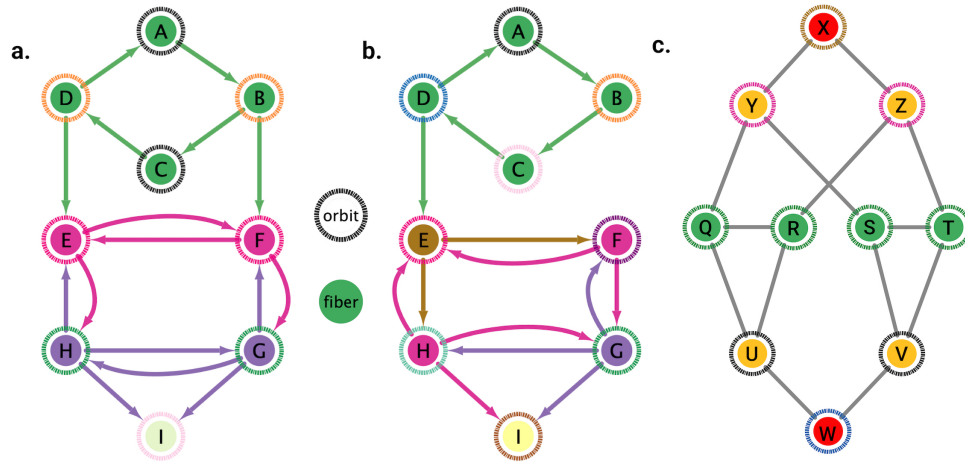


Fig 2. Fiber and orbits. The inner color of a node is a representation of the fiber to which said node belongs to and the color of the ring indicates to which orbit such a node belongs to. a) Graph with 4 fibers and 5 orbits. The separation of fiber and orbits among the 4 upper nodes occurs due to the presence of outgoing edges into nodes E and F. b) This graph only differs from a) by the removal of the edge $B \rightarrow F$ exemplifying how restrictive orbit symmetries are. There are only trivial orbits but there still non-trivial fibers. c) Although it is more common to have a matching of the partitionings produces by fibers and orbit symmetries in a given undirected networks there can exist situations in which these two are not matching as seen in this example. In this simple example there is a breakage between the fiber and orbit symmetries due to the in-existence of a permutation action which could swap nodes X, Y and Z respectively with their fiber symmetric counterparts W, U and V meanwhile preserving its structure and adjacency matrix.

Nodes with the same input tree are in the same *fiber*, which are projections of a morphism called a *graph fibration* [28]. A graph fibration φ between two graphs $G = (N_G, E_G)$ and $B = (N_B, E_B)$ is satisfied when for any $e_B \in E_B$ and any $v_G \in N_G$ with $\varphi(n) = h(e_B)$, there is a unique $e_G \in E_G$ such that $\varphi(e_G) = e_B$ and $h(e_G) = v_G$. A *fiber* is a set of nodes (cluster cell) with isomorphic input trees in G , mapped via φ onto a node in B , where G is the total space and B is the base. This paper focuses on the *minimal graph fibration*, collapsing a graph into its *minimal base*, where the base contains one node for each unique input tree, resulting in a trivial partitioning of B and a *minimal* balanced coloring of G [28]. A partitioning with k cluster cells that obey equitable partitioning is minimal if no other partitioning with fewer than k clusters satisfies the equitable partitioning condition [31]. An example of this can be seen in Fig 3.

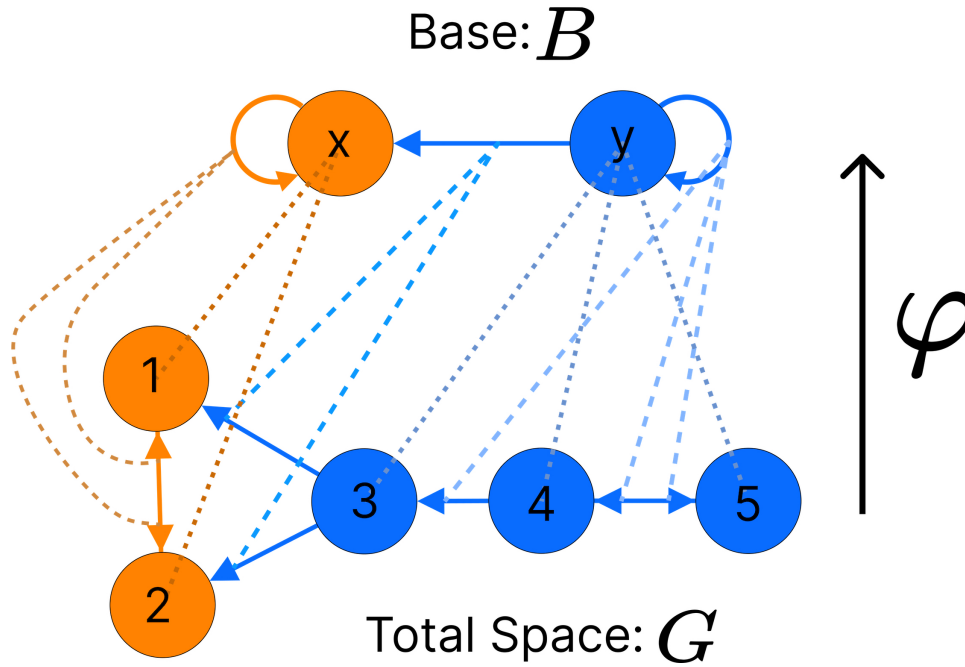


Fig 3. Graph fibration $\varphi : G \rightarrow B$. The network at the bottom (G) shows an example for a graph where the color of its nodes represents the fiber to which they belong. Notice that all nodes with the same (e.g. $\{3, 4, 5\}$) color are collapsed on to one representative node (y) in the network above called the base. This collapsing process is known as the lifting property of a graph fibration φ . This property also applies to edges, notice that the edges in the total space (e.g. $\{e_G^{3 \rightarrow 1}, e_G^{3 \rightarrow 4}\}$) which are lifted to one representative edge in the base which is situated between nodes of the same color as in the total space ($e_B^{y \rightarrow x}$).

Nodes in the same fiber synchronize, meaning that the associated admissible ODEs have the same value at the same time [28, 36]. There are no restrictions on the behavior of nodes in different fibers, and it is possible for two or more fibers to synchronize [27]. Connected nodes in the same fiber may have phase shifts under the same frequency or an integer multiple of a base frequency, but only if the nodes have rotational symmetry, and the phase shift is a rational fraction of 2π [31].

We find the fiber partitioning algorithmically by initially coloring all nodes and arrows with a unique color. After that, the algorithm recolors all nodes with the same number of colored inputs with a new color, including their outgoing arrows. These procedures continue until no recoloring is possible. We apply this method through the algorithm proposed by Kamei & Cock [67] and implement it through the code developed in [38].

Automorphism and their orbit partitioning

The second method relies on the set of automorphisms of a graph, which is a bijective function σ from a graph onto itself preserving the structure of the graph, specifically its adjacency matrix A . The set of all automorphisms of graph G along with the operation of composition forms the automorphism group $Aut(G)$ [68]. Specifically, an automorphism is a permutation of the vertices of the graph that preserves the adjacency relationships between them. If G is a graph with vertices $\{v_1, v_2, \dots, v_n\} \in N_G$ and with

edge set E_G , then an automorphism of G is a permutation σ of the node set such that if (v_i, v_j) is an edge in G so too is $(\sigma(v_i), \sigma(v_j))$ an edge in G . An automorphism function σ can take the form of a symmetric permutation matrix P where matrix is considered to be an automorphism of an adjacency matrix A if the following holds:

$$PAP^{-1} = A, \tag{4}$$

where P^{-1} is the inverse of P . Additionally it is invertible meaning that $P = P^{-1}$ or $PP^{-1} = 1$ allowing Eq (4) to be rewritten as:

$$[P, A] = AP - PA = 0. \tag{5}$$

The permutations of the automorphism group can be grouped into sets that form normal subgroups meaning that a permutation from one set can commute, as in Eq (5), with the permutation of another set (disjoint unions) [34]. In other words, applying one of these permutations to a graph it only permutes a closed set of nodes, leaving the rest of the graph's nodes intact.

If when σ is applied on a graph's adjacency matrix A as in Eq (6) and it doesn't change it, then multiple consecutive applications won't either.

$$\sigma(A) = PAP^{-1} \tag{6}$$

Although an automorphism's consecutive application preserves a graph's adjacency matrix, it does shuffles node labels. So, a node's label always returns to its original after visiting other nodes. Given a graph G and σ , the orbit of node v under σ is the set of all vertices that can be reached by applying σ repeatedly. That is, the orbit of v is the set nodes

$$\{\sigma^k(v) : k \in \mathbb{Z}\} \tag{7}$$

where \mathbb{Z} denotes the integers numbers. The orbit of node v includes all vertices equivalent to v under the action of σ , transformed by applying σ k times. The set of nodes belonging to an orbit are said to have the same *orbit coloring* [32,69] were studies in dynamical systems show that network automorphisms lead to the synchronization nodes in an orbit [31,67,70,71].

Orbit partitioning results from analyzing the complete set of automorphisms of a graph $Aut(G)$. Orbits can be revealed not only by repetitively applying a single automorphism but also by applying the set of automorphisms $Aut(G)$ consecutively in all possible orders and multiplicities (e.g., $P_3P_1P_2P_2$). This approach allows for a wider range of transformable nodes to be detected. The procedure of how this is explicitly done is out of the context of this paper, but the process of uncovering orbit coloring partitions is done using SageMath [72], an open-source mathematics software that utilizes various Python packages, including Nauty [73].

The orbit partitionings that emerge from this are equitable partitioning which are cluster cells, stressing that an orbit coloring is always an equitable partition, but the reserve is generally not true [31,32]. This is because, by definition, orbit partitioning requires the conservation of both in-degree, requested for the equitable partition, and out-degree. As such, an equitable partition may not be an orbit partition since the out-degree condition may not be met.

Fibers vs orbits

As discussed above the equitable partitionings of fibers and orbits are related to the concept of symmetry. The orbits obtained from automorphisms are analogous to the fibers obtained from symmetry fibrations. Orbits, however, are a more restrictive form

of graph symmetry as these must satisfy in-degree and out-degree edge constraints. In contrast, fibers must only satisfy in-degree constraints.

Fibration symmetries in a graph have fewer constraints than automorphisms, resulting in fewer partitionings in the graph. Orbits are a subset of fibration symmetries, which additionally conserve the out-degree structure of the adjacency matrix. This means that every orbit is also a fiber, and the in-degree constraint present in the orbit partitioning, which is the main constraint in fiber partitioning, leads the nodes in the same orbit (cluster cell) to become synchronous [33]. However, note that a fiber is not necessarily an orbit.

In Fig 2a, an example of a graph with three fibers and four orbits is shown. The existence of more fibration symmetries than automorphisms generally leads to having fewer (or equal) fibers than orbits. In other words, having more symmetries implies having fewer cluster cells. The green nodes have the same number of in-degree edges (belonging, therefore, to the same fiber) but some have different number of out-degree edges. Nodes B and D each have an out-degree equal to 2. Another way to conserve the structure of this graph other than applying the identity transformations is by rotating $A \rightarrow B \rightarrow C \rightarrow D \rightarrow A$ twice in this order, and in concurrence reflecting horizontally all the nodes below the green nodes. Without applying this reflection, node B would have one outgoing edge into node E , therefore not preserving the original graph's structure. Notice that any permutation for the upper four nodes would still preserve its fiber symmetry as these would continue to only receive one green in-degree edge.

As an additional example, the removal of edge $B \rightarrow F$ as seen in Fig 2b destroys the orbit symmetry of the graph. No rotation between the upper four nodes would allow node D to have an outgoing edge to node E other than its original position. There also does not exist any permutation of the lower five nodes that would keep the structure intact all due to the removal of $D \rightarrow E$.

Building blocks

Number theory shows that every natural number can be represented as a unique product of prime numbers [74]. Prime numbers are considered the fundamental building blocks of natural numbers. This concept is extended to group theory, where finite groups can be broken down into simple subgroups [75]. This abstract example has implications for natural systems due to the relationship between group theory and symmetry. A similar relationship can be applied to biological networks, as shown in [39, 76–78]. In this paper, we decompose the networks into fundamental building blocks by relying on the symmetries of the fibers and their input trees, as discussed in [26]. Despite the diverse range of input tree topologies, they share common structural characteristics that allow us to categorize all fibers into distinct and succinct fiber building blocks (FBBs).

The input tree's structure can be represented by a sequence a_i that denotes the number of nodes in layer i . This sequence also corresponds to the number of paths extending to the single node at layer 1, the root of the input tree. The *branching ratio*, or common ratio, can be found by taking the limit of a_{i+1}/a_i as $i \rightarrow \infty$. This ratio is denoted by $|n\rangle$ and represents the number of loops in the input tree. The fiber number $|n\rangle$ can be an integer or an irrational number, with the latter indicating complex branching due to nested loops, which are referred to as "Fibonacci fibers." One other property that is used to characterize an input tree of a node is the number of unique simple paths with no repeating edges which terminate on such. The number of paths is calculated in the base graph induced by the nodes that compose the input tree disregarding edge multiplicity between nodes. This property is symbolized by $|\ell\rangle$ and together with $|n\rangle$ are enough to categorize the topology of input trees where the two can be agglomerated into $|n, \ell\rangle$ which are called *fiber numbers*.

Here in this paper we show the building components of the chemical networks. In order to do so and explain it in a more detail manner each of the networks will be broken into multiple sub-graphs. These sub-graphs of the chemical network are induced by all the unique nodes present in the input tree for all nodes in a same fiber. We refer to these sub-graphs as *circuits*. Each of these circuits are broken into multiple FBBs which when "added" together form the circuit.

For each fiber in a graph there exists a fiber building block (FBB) associated with it which is a sub-graph $S \subseteq G$ induced by the following nodes [26]:

- all the nodes in the fiber,
- immediate in-degree neighboring nodes of all the nodes in the fiber,
- nodes belonging to the shortest loop that include a node in the fiber which are not a self-loop,
- if all points above lead to two or more disconnected graphs, the nodes composing the shortest path connecting each pair of disconnected graphs are included. These types of FBBs are dubbed composite fiber building blocks which are further explained below.

For all nodes that are considered in the second point above we refer to these as regulatory nodes. If the nodes in the fiber are found to send information back into the fiber then these too are considered as regulatory nodes.

Simpler fiber building blocks can be combined to create multilayered composite blocks needed when the topology of a circuit or FBB cannot be fully captured by one fiber number pair $|n, \ell\rangle$. In such cases, the $|n, \ell\rangle$ of the input tree of each regulator of an FBB is added to the $|n, \ell\rangle$ of the input tree of the FBB itself, creating an addition between two adjacent layers. This addition is performed in a left-to-right ordered sequential manner, resulting in the following formulation:

$$|n_1, \ell_1\rangle \oplus |n_2, \ell_2\rangle + |n_3, \ell_3\rangle \oplus \dots \quad (8)$$

The symbol \oplus represents an addition of FBBs between adjacent layers and the symbol $+$ is used to indicate that the two FBBs next to this symbol are in the same layer. In the example above the fiber number $|n_1, \ell_1\rangle$ represents the FBB at the first layer. Fig 4 shows an example of multilayered FBB composed of regular and Fibonacci building blocks. Located in the second and third layers are Fibonacci building blocks which are composed of nested loops. Take as an example the Fibonacci building block located in the second layer which has loops of different lengths, particularly of length 2, 3, and 4 of which each is nested in the other. Overall these types of combination of fiber building blocks aid in determining the order of complexity among fibers.

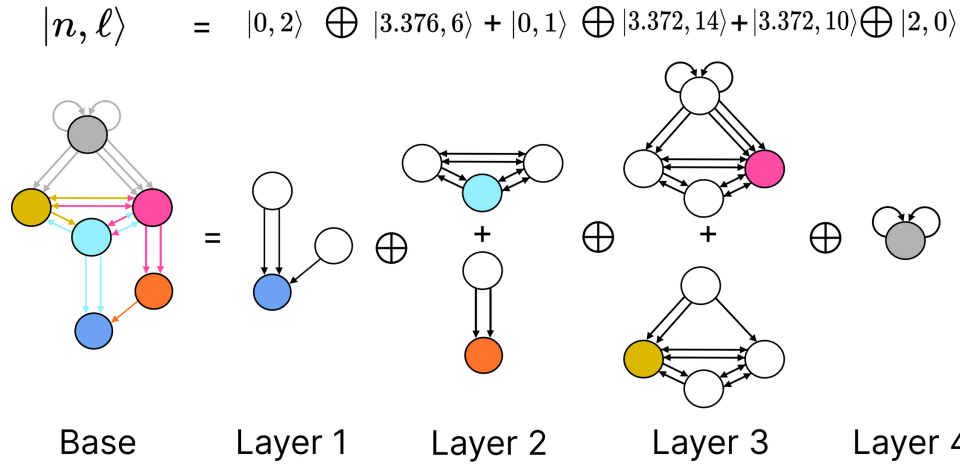


Fig 4. Fiber building block decomposition. Present here at the most left is the base of the circuit induced by the input tree for the fiber containing neurons DA05, DA08, DA09, VA09, and VA11 (blue node) present in the backward chemical network as seen in Fig 7.a with the same color scheme. The first input into this fiber are provided from the orange (VA12) and cyan (AVD) nodes where these form the first layer of the multilayered block. The input tree of the network formed by these nodes give a fiber number of $|0, 2\rangle$ ($\ell = 2$ as multiplicity of edges are ignored). The next layer is composed by the elementary fiber building blocks of the input fibers in the previous layer. This notion is carried out at every layer until all fibers have been shown only once. Layer 2 already shows a complex elementary FBB for the cyan node with fiber numbers $|3.376, 6\rangle$. Layer 3 too contains elementary FBB with a similar fiber number as the cyan node in layer 2; the only difference here is that these two contain different number of inputs therefore the ℓ number is different in these two. Additionally in layer 3, self-loops of the gray node are present for the upper elementary FBB as the nodes forming this fiber are composed by neurons AIB and RIM which form a square network and which all send signals to the pink fiber. As for the gray fiber in the elementary FBB at the bottom it is only formed by neurons AIB which have no connections between them and therefore their collapse does not produce self-loops. The fiber building block induced by the input tree of the blue fiber concludes with a 4th layer which contains 4 neurons connect in a square. These have no external input which leads to it having fibers numbers $|2, 0\rangle$ which captures the duplication of nodes at each layer in their input tree.

Admissible ODEs

We compare results of fiber and orbits with cluster synchronization obtained from simulating interacting neurons. Interactive nodes are simulated by mapping admissible in-degree dependent coupled ordinary differential equations (ODE) of the form in Eq (9) to each node in our networks [28, 30, 31, 36, 71]. The i -th neuron's input is the i -th column of an adjacency matrix \tilde{A} , where the j -th row in the column represents the strength of the input from neuron j to neuron i , and this strength is the weight of the edge from neuron j into neuron i .

$$\frac{dV_i}{dt} \equiv \dot{V}_i = \mathbf{f}(V_i) + \tilde{\sigma} \sum_{j=1}^n \tilde{A}_{ji} \mathbf{g}(V_i, V_j) + \sigma^{ext} I_i^{ext}, \quad i = 1, \dots, n \quad (9)$$

Each i -th neuron of a network has a voltage V_i associated with it, representing the membrane potential of the i -th neuron. The rate of change of this voltage V_i is given by

an ODE of the type in Eq (9). As the equation shows, V_i is affected by the voltage of other neurons coupled with it with a strength associated with the sum on the right side of Eq (9).

To emulate the activation of neurons involved in the forward or backward locomotion of *C. elegans*, our models provide external stimuli through the term I_i^{ext} to only some neurons in each network. This action is called driving or stimulating the network. The left and right versions of an inter-neuron pair, which govern the activation of the downstream motor-neurons DA, DB, VA, and VB responsible for activating wall muscles that produce locomotion, are mainly selected to receive the external stimuli through I_i^{ext} [50]. All nodes without external input stimuli have their I_i^{ext} set to zero. The time constants represented by the symbol σ control the rate of change of the ODE components.

The smooth internal state function $\mathbf{f}(\cdot) : \mathbb{R} \rightarrow \mathbb{R}$ and pairwise interaction function $\mathbf{g}(\cdot, \cdot) : \mathbb{R} \times \mathbb{R} \rightarrow \mathbb{R}$ can be either linear or nonlinear, and are present for both types of interactions in the *C. elegans*: chemical synapses and gap junction interactions. The gap junction interaction function is linear, while the chemical synapse interaction function is nonlinear. The internal state function $\mathbf{f}(\cdot)$ brings a neuron back to its resting state voltage V_{rest} . For the chemical synapse interactions, two types of functions are explored: the Chem type I model based on [79,80], and the Chem type II model taken from [81–83]. These lead to three types of ODE interactions applied to their corresponding networks:

$$\dot{V}_i = \mathbf{f}(V_i) - \alpha^{gap} \sum_{j=1}^n \tilde{A}_{ji}^{gap} (V_i - V_j) + \alpha^{ext} I_i^{ext} \quad \text{Gap junction} \quad (10)$$

$$\dot{V}_i = \mathbf{f}(V_i) - \alpha^{chem} \sum_{j=1}^n \tilde{A}_{ji}^{chem} \Phi(V_j) (V_i - V_{s,j}) + \alpha^{ext} I_i^{ext} \quad \text{Chem type I} \quad (11)$$

$$\dot{V}_i = \mathbf{f}(V_i) - \alpha^{chem} \sum_{j=1}^n \tilde{A}_{ji}^{chem} s_j (V_i - V_{s,j}) + \alpha^{ext} I_i^{ext} \quad \text{Chem type II} \quad (12)$$

with support functions:

$$\mathbf{f}(V_i) = -\alpha^{leak} (V_i - V_{rest}) \quad (13)$$

$$\frac{ds_i}{dt} \equiv \dot{s}_i = a_r \Phi(V_i) (1 - s_i) - a_d s_i \quad (14)$$

$$\Phi(V_i) = \frac{1}{1 + \exp\{-\gamma(V_i - V_i^{threshold})\}} \quad (15)$$

$$I_i^{ext} = I_{drive} + I_{osc} \sin 2\pi ft + I_{noise} \quad (16)$$

The term I^{ext} in Eq (16) consists of three parts: I_{drive} is a positive constant current; I_{osc} is an oscillatory term and a Gaussian random walk term I_{noise} (with standard deviation of 1 scaled between $0.1pA$ to $-0.1pA$). The oscillatory stimuli frequency of the driven neurons was selected between 1Hz to 3Hz to approximate the swimming frequency of an adult wild-type *C. elegans* in agar [84]. The external stimuli function I^{ext} was enforced to be the same for neurons with the same balanced coloring as to preserve their input symmetry.

Finally the models used here do not have time delays to represent the finite time of signal propagation between neurons, it has been shown that neuron ODE models can

still synchronize when this effect is taken into consideration [65]. Additionally the parameters used and explained below need not be exactly the same between neurons for synchronization to occur, although it can reduce the system's capacity to achieve synchronization [66].

ODE parameters and implementation methods

The parameters of these ODEs shown above are taken from Kunert *et al.* [82]. The parameter α^{leak} is a time constant with a value of $10s^{-1}$ and is associated with the rate of decay of the neuron's membrane potential. This is derived from the leakage conductance per surface area g_L times the average surface area of an inter-neuron S (based on Varshney [8] $g_L \cdot S$ is equal to $0.01nS$) divided by the membrane capacitance of a neuron (Varshney *et al.* [8] defines C to be $1pF$). The time constants for chemical synapses and gap junctions have the same value of $g_L \cdot S/C = 0.1nS/1pF = 100s^{-1}$ where these fall within the value range from Koch's book on biophysics [85].

The constant γ is associated with the steepness of the sigmoid function which is set to $2\ln(0.1/0.9)/36mV$ in accordance to Wicks *et. al* [51], which defines this constant to be representative of a change of the value of the sigmoid function between 0.1 to 0.9 within a range of $36mV$. This value is close to that reported by Kunert [82] so it is rounded to $125V^{-1}$ to match Kunert's value.

The terms $a_r = 1s^{-1}$ and $a_d = 5s^{-1}$ associated with the Chem type II model correspond to the synaptic variability's rise and decay times [82]. The equilibrium value for the synaptic variability term comes from setting Eq (14) to zero and having the sigmoid equal to 0.5; this leads to a value of $s_{eq} = ar/(ar + 2 * ad) = 0.09$. Finally α^{ext} is simply set to $1/C$ and $V_{s,j}$ takes two values: $0mV$ for excitatory vs $-70mV$ for inhibitory presynaptic neurons [86]. For this study, we considered all chemical synapse connections to be excitatory (although our code accepts networks with inhibitory connections). The units of I^{ext} are pA to match the units (V/s). All neurons in the simulation conducted in this paper have the same parameters as the different families of motor-neurons are known to be the most similar among all the differently distinct electrophysiological group of neurons [47]. We extend this notion to the parameters of the interneurons to have a simpler system to work with, as well due to the nature of our sub-networks being mainly composed by motor-neurons.

We set the threshold voltage $V^{threshold}$ for each neuron to the corresponding solution obtained by setting Eq (11), Eq (12), and Eq (14) to zero and Eq (15) to 0.5; where the solution is the stable point solution for this ODE model. This procedure (Gaussian elimination) is similar to that in Wick *et al.* [51] where in such I_i^{ext} is set to 0 where as we set it to I_{drive} (the mean value of an undulatory or of a noise stimuli is 0, therefore, these are not included). This recipe finds the solution of the threshold voltage to be the one below

$$V^{threshold} = A^{-1}b \quad (17)$$

such that A is given by

$$A_{ii} = 1 + \frac{1}{\sigma_{leak}} \sum_{j=1}^n (\sigma^{gap} \tilde{A}_{ji}^{gap} + c\sigma^{chem} \tilde{A}_{ji}^{chem}) \quad (18)$$

$$A_{ji} = -\frac{1}{\sigma_{leak}} \sum_{j=1}^n \sigma^{gap} \tilde{A}_{ji}^{gap}$$

and b by

$$b_i = V_{rest} + \frac{1}{\sigma_{leak}} \left(\sum_{j=1}^n c\sigma^{chem} \tilde{A}_{ji}^{chem} V_{s,j} + \sigma^{ext} I_i^{ext} \right). \quad (19)$$

where the term c is equal to s_{eq} for the Chem type II model or 0.5 for the Chem type I model. It is important to point out that threshold voltage is respectful of the in-degree nature of Eq (9). Further in the paper $V^{\text{threshold}}$ is used in conjunction with the Jacobian to determine the stability of the solutions.

The ODE dynamics were evolved and computed using the Runge-Kutta-4th method with a time step dt of 0.1 milliseconds. Noise dynamics were implemented through a modified stochastic Runge-Kutta method as proposed in [87], where the update time step for the noise is $dt^{1/2}$. A link to a user-friendly Matlab app developed in-house can be found in the Data and code section. This app can reproduce any of the dynamics presented in this paper with the appropriate inputs. It can measure the level of synchronization (explained in the next section) and has additional tools for further experimentation.

Synchronicity measure

Synchronicity can be quantified in several ways, including Pearson correlation, covariance, and cross-correlation. However, we propose a stricter metric based on the potential of two neurons i and j being fully synchronous if they have the same value within a certain time window as defined in Eq (20).

$$V_i(t) = V_j(t) : \forall t \quad (20)$$

To measure near-full synchronicity and distinguish between distinct potentials, we introduce the Level of Synchronicity (LoS), which utilizes a time-averaged Gaussian kernel distance [88]. The LoS metric enables us to differentiate between situations of nearly equal potentials and those with no synchronicity at all.

$$LoS_{ij} = \frac{1}{T} \sum_{t=\text{time step}}^T \exp\left\{-\frac{[V_i(t) - V_j(t)]^2}{2\sigma^2}\right\}. \quad (21)$$

In the equation above, T is the total amount of time steps on which LoS is applied between the signals of neurons i and j . The range of the LoS function is $[0, 1]$ where a value of 1 indicates full synchronicity, whereas a value of 0 would indicate no synchronization. The parametric term σ serves as a scale to define a benchmark for closeness between two points.

To apply the LoS metric to our simulations, we allow each network to reach a stable state after the initial transients by running it for a sufficient amount of time. We use the last second of simulation time to determine the synchronicity level, analyzing all pairs (i, j) and producing an LoS matrix for each network simulation. We use a value of $\sigma = 0.1mV$ for all simulations, such that a potential difference of $0.1mV$ between two neurons over a time window T would yield an LoS value of approximately 0.61. We chose σ by starting at $10mV$, which produced a fully synchronous LoS matrix for all networks and ODE models with no external stimuli. We then reduced σ until the average of all LoS pairs between two fibers in the network with the most fibers was below 0.001.

Besides the LoS measure, we used the Phase Locking Value (PLV) [89] measure at our last set of simulations to measure the amount of phase synchronicity. PLV quantifies the degree of synchronization or coupling between two undulatory signals. It is based on the idea of the difference between the instantaneous phase of two signals at each time point, and then computing the average over a certain time window. These values fall between 0 and 1, where 1 indicates two signals are in constant phase synchronicity (the two signals hold the same phase difference through a recording). A value of 0 indicates that the two signals have varying phases such that the difference between these is random and does not remain constant.

Results

Network partitions in the locomotion connectome

We focus on the forward gap junction (F-Gap), backward gap junction (B-Gap), forward chemical synapses (F-Chem), and backward chemical synapses (B-Chem) taken from [37] where each one of these are binary edges networks. In addition we also work with the integer edge weighted version of the aforementioned networks that respect the symmetrization done in [37] and their fiber partitionings. For the latter the weight of an edge between two fibers was taken to be the rounded-up integer of the average of all the edges present in the original connectome of [8] between the cluster cell of the fibers under consideration.

The resulting partitionings and their cluster cells are the same for both binary and integer weighted networks since the graph structure \mathcal{G} is the same regardless of edge type. However, the input tree for a fiber associated with a specific neuron is likely different between binary and weighted versions.

Additionally the adjacency matrix for each of the integer edge weighted networks is preserved under the permutation actions of the normal subgroups of the $Aut(\mathcal{G})$ of the respective binary network [37]. Notice that, in principle, automorphisms of weighted networks are different from automorphisms of binary networks: one weighted edge can easily break the symmetry of a binary network. As such, in a weighted network, the permutation needs to conserve adjacency taking into considering their weights. Due to the way the integer edge-weighted network has been constructed the orbits of the binary and integer edge-weighted networks are the same, meaning that the repetitive application of the same permutation on both the binary and integer versions of a network will result in a group of neurons visiting the same nodes of the network.

Fig 5, Fig 6, and Fig 7 show the results of the partitioning for the four different graphs under analysis. Fiber and orbit partitionings are the same for the forward and backward cases of the undirected gap junction networks (Fig 5b and Fig 6 respectively). This is a direct consequence of the bidirectionality nature of undirected graphs where two nodes with the same fiber symmetry also preserve out-degree edges. Indeed, in an undirected graph, the in-degree (conditions for fibers and orbits) and the out-degree (condition for orbits) of a node has the same value. That is, every undirected link can be seen as an in and out-directed link, therefore, preserving the in-degree connectivity generally implies also preserving the out-degree, and therefore, the fibers can be expected to be the same as the orbits.

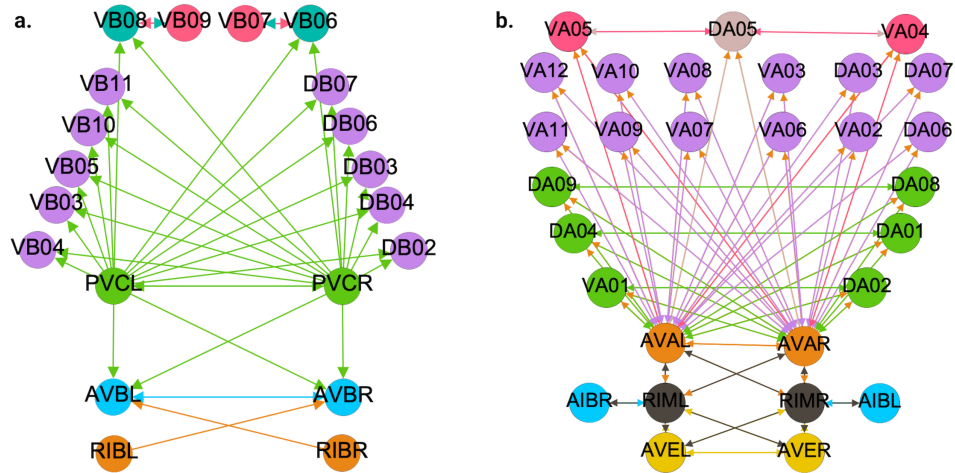


Fig 5. Partitioning results for the F-Chem and B-Gap networks. Results for the minimal balanced coloring and the orbit coloring are same for these 2 networks. The colored shaded areas show the normal subgroups that form the automorphism group of these graphs ($Aut(\mathcal{G})$) with their respective symmetry groups represented by the same colored symbol. (A) The F-Chem network has its 22 neurons partitioned into 4 distinct colors. (B) The B-Gap network with its 29 neurons partitioned into 6 distinct synchronous groups.

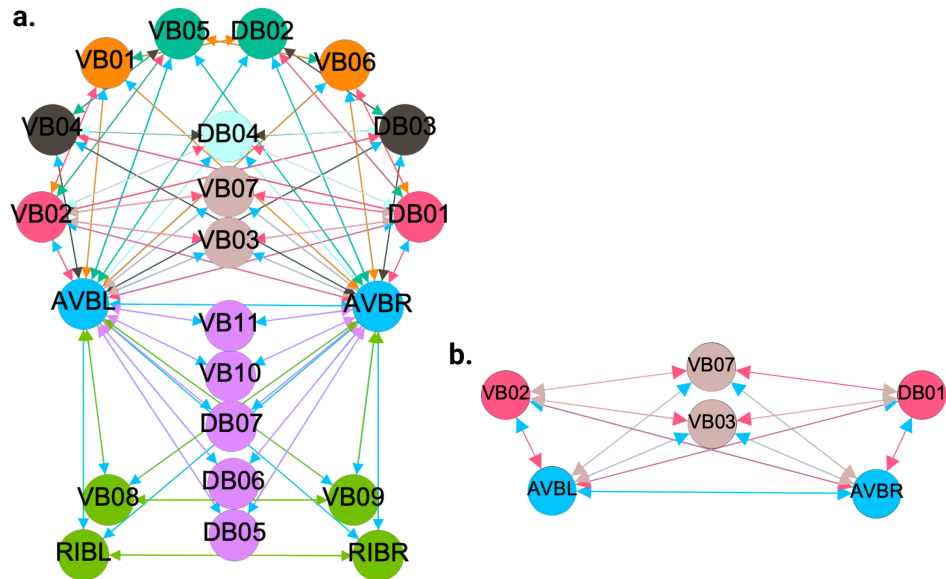


Fig 6. Partitioning results for the F-Gap network. Results for the minimal balanced coloring and the orbit coloring are same for this network. The colored shaded areas show the normal subgroups that form the automorphism group of these graphs ($Aut(\mathcal{G})$) with their respective symmetry groups represented by the same colored symbol. (a) The F-Gap network with its 20 neurons partitioned into 6 distinct equitable partitions with one partition containing only one neuron. (b) Sub-graph used as a visual aid for the example found in the Network partitions in the locomotion connectome section.

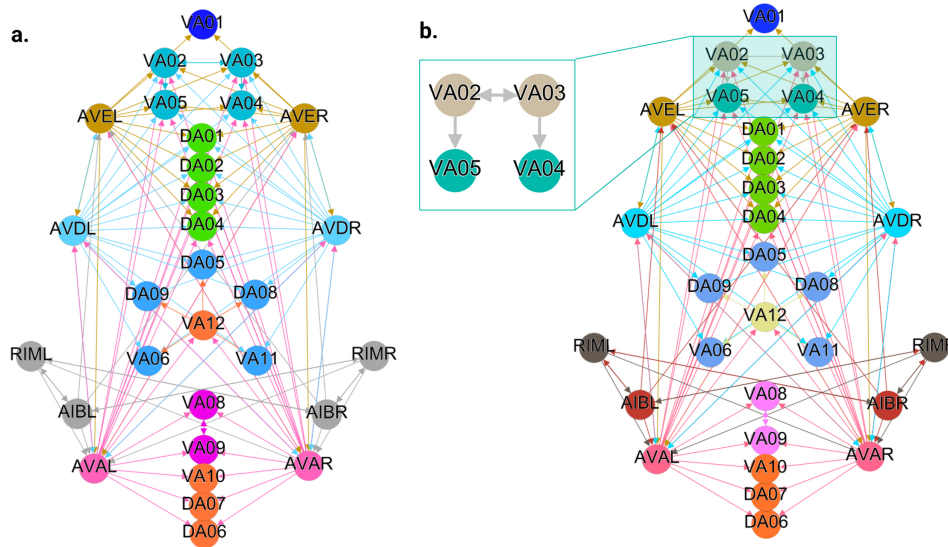


Fig 7. Backward Chemical synapses network (B-Chem) partitioning results. The partitioning of nodes into different synchronous groups is depicted by the color of the nodes. (A) The minimal balanced coloring results show 10 distinct colors/partitions for the 30 neurons involved. (B) The orbit coloring results for this network where the 30 neurons have been partitioned into 13 distinct partitions. The colored shaded areas show the normal subgroups that form the automorphism group of this graph ($Aut(\mathcal{G})$) with their respective symmetry group represented by the same colored symbol. (C) An example of neurons with different minimal balanced coloring and orbit coloring. The latter has a permutation symmetry S_2 swapping VA02 with VA03 and VA05 with VA04 simultaneous which preserves the structure of this network.

We emphasize that this is not always true. We can think of many cases of undirected networks where fibers are not the same as orbits, see Fig 2c. In this simple example, there is a breakage between the fiber and orbit symmetries due to the in-existence of a permutation action that could swap nodes X, Y, and Z, respectively, with their fiber symmetric counterparts W, U and V meanwhile preserving their structure and adjacency matrix. However, it is interesting that we find that in the gap junctions, the orbit partitionings equal the fiber partitionings, and fibrations symmetries do not add any more to what we can find with the automorphisms of these networks. Thus the structure of the gap is enough to be characterized by automorphisms [37] completely characterize these networks. In [37], we stop the analysis at the level of automorphisms, whereas here, we also find the associated orbits and their fiber building blocks.

The situation is different when the graph is directed, and as such, the in-degree of a node may differ from its out-degree. In these circumstances, the less stringent constraints of Fibrations result in a higher number of symmetries and, therefore, a smaller number of fibers. Orbit and Fiber partitionings can also be the same in (directed) networks. These are equivalent when the automorphism group of the graph acts transitively on the set of fibers. Meaning that all the nodes of a fiber (for all fibers) should be able to be permuted with one another under the action of a permutation symmetry in the automorphism group of the graph [90].

In the F-Gap network (Fig 6), nodes VB03 and VB07 are an example where they have bidirectional connections with both AVBL and AVBR inter-neurons and DB01 and VB02 motor-neurons. They belong to the same fiber and orbit. If VB07 did not have out-going connections to the inter-neurons (AVBL and AVBR), and if VB03 did not

have out-going connections to the motor-neurons (DB01 and VB02), then the fiber partitioning would remain the same. However, the orbit coloring would partition neurons VB03 and VB07 into their own unique colors since no permutation between these two nodes would preserve the connectivity matrix of the network. The minimal balanced coloring and orbit coloring are also the same for the F-Chem network, as the minimal balanced coloring for this particular network is modular and out-degree conserving in each of its partitions.

In contrast to other networks, B-Chem (Fig 7) exhibits differences between minimal fiber and orbit coloring. Consider the example of neurons VA02, VA03, VA04, and VA05 shown in Fig 7c, where each node receives the same number of inputs from inter-neuron pairs AVE, AVD, and AVA. Any permutation among these nodes preserves the number of colored inputs they receive, resulting in the same fiber (minimal balanced coloring). However, node VA04 has no outputs, so permuting VA03 with VA04 would change the adjacency matrix of the sub-graph. The only way to preserve the out-degree of these four nodes under permutation is to simultaneously permute VA02 with VA03 and VA05 with VA04 ($\{\{VA02, VA03\}, \{VA04, VA05\}\}$), which is an instance of an orbit coloring.

Another example of differences between the minimal fiber partitioning and orbit coloring partitioning can be observed for VA12 and between L-R inter-neurons RIM and AIB. Besides the latter example, in all four networks, left-right inter-neurons pairs belong to their own unique partitioning.

Fiber building blocks

The FBBs of the F-Chem are categorized by integer n and low ℓ values, and are driven solely by neurons PVCL and PVCR. The first row of Fig 8 shows the only multilayered composite building block with fiber numbers $|1, 1\rangle \oplus |1, 2\rangle$, which represents VB07, VB09 and VB06, VB08, respectively.

FBB	FBB Base	Input tree	Neurons	$ n, \ell\rangle$
			VB09 VB07	$ 1,1\rangle$ \oplus $ 1,2\rangle$
			VB08 VB06	$ 1,2\rangle$
			DB02 VB03 DB03 VB04 DB04 VB05 DB06 VB10 DB05 VB11	$ 1,1\rangle$
			AVBL AVBR	$ 1,2\rangle$
			PVCL PVCR	$ 1,0\rangle$
			RIBL RIBR	$ 0,0\rangle$

Fig 8. Forward Chemical Fiber Building Blocks. Left column illustrates all the building blocks that form the binary F-Chem network. These sub networks arise as a consequence of its neurons belonging to a unique strongly connected component and all neurons with outgoing edges to it. The column named Fiber Base shows the collapsed version of the building block where numbers indicated the number of arrows between two nodes. The input tree here is a visual capturing of all the paths in the network in which the final node is part of the fiber under focus. The right most column features the "fiber numbers" $|n, \ell\rangle$ associated with each particular fiber. n indicates the number of unique infinite paths and ℓ captures the number of "regulators" which are the neurons that only have out-going edges which form part of the input tree.

The backward chemical network is composed of Fibonacci FBBs, formed by third layer interneurons AVA, AVD, and AVE, which receive information from first and

second layered interneurons AIB and RIM [91] to form a loop circuit, as depicted in Fig 9. The branching ratio of Fibonacci FBBs in the backward chemical network is 3.3723..., which was not observed in a previous study of the *E. coli*'s genetic network under this analysis [26]. This suggests a higher complexity in the neuronal circuitry of *C. elegans* compared to the genetic network of *E. coli*. Regardless, a FBB with an irrational number for $|n\rangle$ indicates that the block is composed of nested loops. In the case of Fibonacci building blocks, these have nested loops of length 2, 3, 4, and up to 5, as shown in Fig 4 at layers 2 and 3 where these form the elementary FBBs of the circuit for neurons DA05, DA08, DA09, VA06, and VA11 (same fiber).

Circuit	FBB Base	Input tree	Neurons	$ \varphi_d, \ell\rangle$
			AIBL AIBR RIML RIMR	$ 2,0\rangle$
			AVDL AVDR	$ 2,0\rangle$ \oplus $ 3.372,14\rangle$ $+ 3.372,10\rangle$ \oplus $ 3.372,6\rangle$
			VA01	$ 2,0\rangle$ $+ 3.372,14\rangle$ $+ 3.372,6\rangle$ \oplus $ 3.372,10\rangle$ \oplus $ 0,1\rangle$
			VA02 VA03 VA04 VA05	$ 2,0\rangle$ \oplus $ 3.372,14\rangle$ $+ 3.372,6\rangle$ $+ 3.372,10\rangle$ \oplus $ 1,3\rangle$
			DA01 DA02 DA03 DA04	$ 2,0\rangle$ \oplus $ 3.372,14\rangle$ $+ 3.372,6\rangle$ $+ 3.372,10\rangle$ \oplus $ 0,3\rangle$
			DA05 DA08 DA09 VA09 VA11	$ 2,0\rangle$ \oplus $ 3.372,14\rangle$ $+ 3.372,10\rangle$ \oplus $ 3.372,6\rangle$ $+ 0,1\rangle$ \oplus $ 0,2\rangle$

Fig 9. Backward Chemical Fiber Building Blocks. Left column illustrates all the building blocks that form the binary B-Chem network. These sub networks arise as a consequence of its neurons belonging to a unique strongly connected component plus all neurons which have out-going edges to such neurons in the strongly connected component. Starting from the third row many of the networks nodes are contained in a box where some of these have out-going edges indicated by the edges outside of the box. The column named Fiber Base shows the collapsed version of the building block where numbers indicated the number of arrows between two nodes (not fully captured in the first column). The input tree here is a visual capturing of all the paths in the network in which the final node is part of the fiber under focus. The last 3 input trees are omitted as these are too big to be figured here. The right most column features the "fiber numbers" $|n, \ell\rangle$ associated with each particular fiber. n indicates the number of unique infinite paths and ℓ captures the number of "regulators" which are the neurons that only have out-going edges which form part of the input tree. Many of the fibers in this network are composite meaning that they are built from the "stacking" of multiple fibers.

The nested loop FBBs composed of AVA, AVD, and AVE can be compressed into smaller and simpler representational graphs using the Fibonacci base. For instance, the FBB associated with $|3.372, 6\rangle$ at the second layer of the network found in Fig 4 can be lifted through a graph fibration to the graph at the 8th row from the top of Fig 10. In this case, neurons AVD (cyan) and AVE (bronze) are collapsed onto one node that produces a self-loop as seen in the Fibonacci base, where the common ratio of the sequence a_n produces a branching ratio of 3.372 for all nodes composing this network. Any FBB with a Fibonacci branching ratio can be compressed into a simpler graph, and therefore have a simpler sequence associated with it.




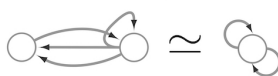

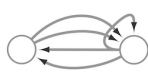




Fibonacci base	Branching ratio	Sequence
	1.0	$a_n = a_{n-1}$
	1 if n is odd 2 if n is even	$a_n = 2 * a_{n-2}$
	1.618...	$a_n = a_{n-1} + a_{n-2}$
	2.0	$a_n = a_{n-1} + 2 * a_{n-2}$
	2.302...	$a_n = a_{n-1} + 3 * a_{n-2}$
	2.561...	$a_n = a_{n-1} + 4 * a_{n-2}$
	3.0	$a_n = a_{n-1} + 6 * a_{n-2}$
	3.372...	$a_n = a_{n-1} + 8 * a_{n-2}$
	3.541...	$a_n = a_{n-1} + 9 * a_{n-2}$
	4.0	$a_n = a_{n-1} + 12 * a_{n-2}$

Fig 10. Fibonacci bases. The graphs presented here are the smallest possible, consisting of only two nodes, capable of producing an irrational common ratios. Additionally each of the examples above have a Fibonacci recursive sequence formula associated with them; reason for calling them Fibonacci bases. If any of the two nodes in these networks receive additional input from external nodes the recursive formula along with its branching ratio are not affected, although their sequences will differ. Due to this larger networks can be collapsed into one of these and still retain the same common ratio. As an example the elementary building block of the cyan node in Fig 4 has the same branching ratio of 3.372... as the Fibonacci base on the 8th row. This elementary building block can be collapsed via a graph fibration into the Fibonacci base previously mentioned; ultimately yielding that the two networks are composed of the same fibers with isomorphic input trees having the same branching ratios. The building blocks in the 3rd layer of Fig 4 have additional inputs emanating from external nodes which prohibits these to be transformed into the Fibonacci base previously mentioned via a graph fibration. Surprisingly these have the same branching ratio, the external inputs only change the initial numbers in the sequence these produce.

Network simulations

In this section, we perform numerical simulations according to the specified ODEs in the Admissible ODEs section and compare their outcomes to those predicted by Orbits and Fibers partitionings.

Simulation test 1 We set all neurons to the same initial voltage value of $-35mV$ without external stimuli, which can be representative of a *C. elegans* during a state named lethargus. During this state, neurons such as ALM have shown low spontaneous activity and remain near their resting state [92]. The initial voltages are normally distributed around the resting state, with the standard deviation varied from 0 to 0.1. We applied this procedure to both types of chemical synapse models. We did not show results for the gap junction networks without external stimuli as they become globally synchronous, with nodes having a voltage equal to the resting state, due to nodes being able to be reached by any other node in the graph. For the Chem type II model, the standard deviation of the synaptic variable varied from 0 to 0.1 with a mean of s_{eq} for every distribution of initial voltages. This setting allowed us to study the effects of the initial syntactic variables on the outcomes of synchronicity and inspect its stability.

Simulation test 2 For the second simulation test, we look into the synchronizations that arise in the networks under external stimuli as modeled by the ODEs found in the Admissible ODEs section. Contrary to the previous case, this setting allows us to explore if these symmetrical neural models of the *C. elegans* synchronize to the predicted partitionings found via fiber partitionings or those of the orbit partitionings for the B-Chem network in an active state of the worm. Before all this a stability analysis to determine the range at which the external stimuli do not induce any instabilities in these networks + ODE models is conducted.

Simulation test 3 We studied four networks and their binary/integer edge-weighted versions. \tilde{A}_{ji} entries in Eq (9) were altered by subtracting a normally distributed value with increasing standard deviation and zero mean. Initial values were set to equilibrium/resting state to assess partitioning method reliability when edge weights are distorted. During our analyses, we kept the σ of the *LoS* function equal to $0.1mV$.

Simulation test 1

Applying the *LoS* measurement to the last second of simulation time for each case produces blocks of synchronicity as seen in Fig 11 and Fig 12. For all the 4 cases pertaining to the backward chemical network, all of the expected fiber partitionings are present (diagonal boxes delineated by red). We find that for the binary version of the backward chemical network, neurons within the same fiber became synchronous with nodes on other fibers, as an example, the 1st and 6th of these diagonal blocks starting from the top in Fig 11. We confirmed that these synchronizations are still present for longer simulation times or with a more restrictive σ parameter. These were only confirmed to be significantly diminished when the networks were driven through an external sinusoidal or Gaussian random walk stimulus, as shown in the **Simulation test 2**.

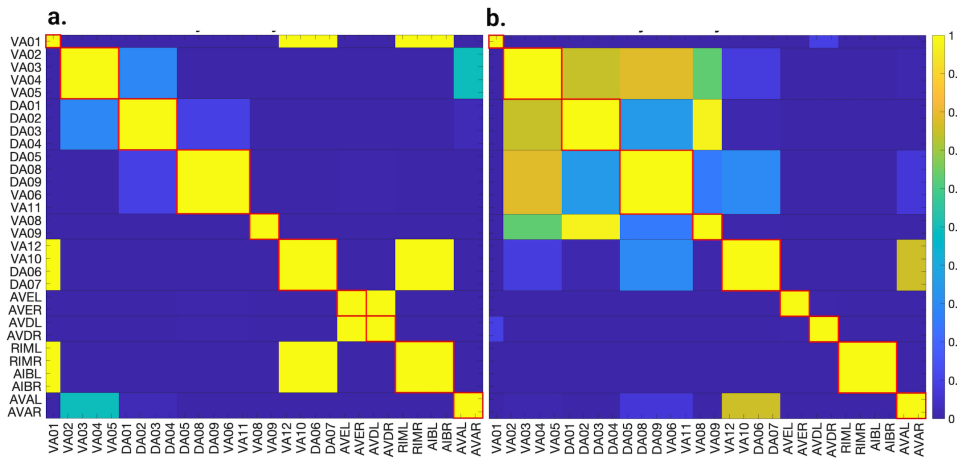


Fig 11. Backward chemical model type I simulations with no external stimuli. Initial voltages set to $-35mV$. a) Left side pertains to the binary version of this symmetric network where an example of two synchronous fibers can be observed (AVDL+AVDR with AVEL+AVER) besides another example with 3 synchronous fibers. An equitable partitioning alone can not predict which fibers become synchronous with one another. b) the right is the weighted version of this system which shows a perfect separation of the values of the nodes into the expected those from fiber partitioning. The block system shows the result of the *LoS* measurement done on the last second of the simulations. The red-lined boxes are visual indicators for the expected cluster synchronization of neurons predicted by the fiberation partitioning method.

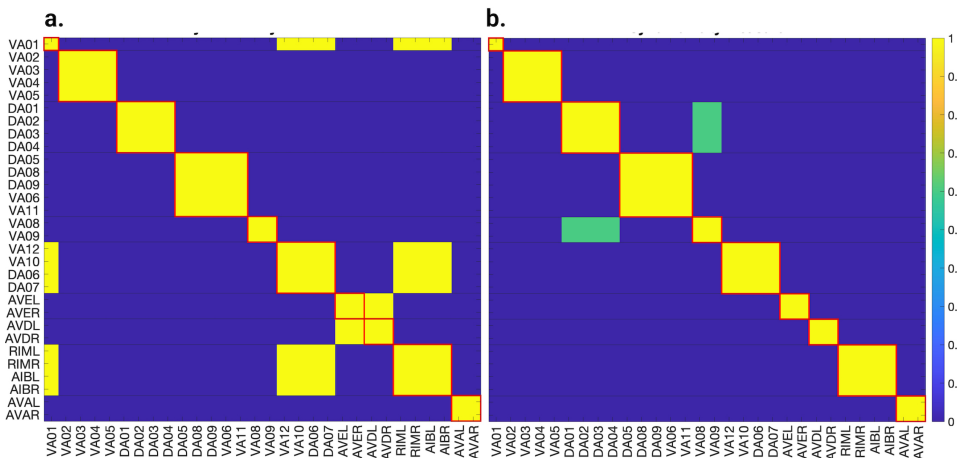


Fig 12. Backward chemical model type II simulations with no external stimuli. Synaptic variables initially set to s_{eq} and initial voltages set to $-35mV$. a) Left side pertains to the binary version of this symmetric network, while the right b) is the weighted version of this system which shows a perfect separation of the values of the nodes into the expected those from fiber partitioning. The block system shows the result of the *LoS* measurement done on the last second of the simulations. The red-lined boxes are visual indicators for the expected cluster synchronization of neurons predicted by the fiberation partitioning method.

Results for the forward chemical model were similar and can be seen in Fig 13. The

forward chemical networks synchronize to the predictions made by the fiber and orbit coloring. In the binary Chem type II case inter-neurons PVC and motor-neurons VB07 and VB09 synchronize as tested by more intensive simulations.

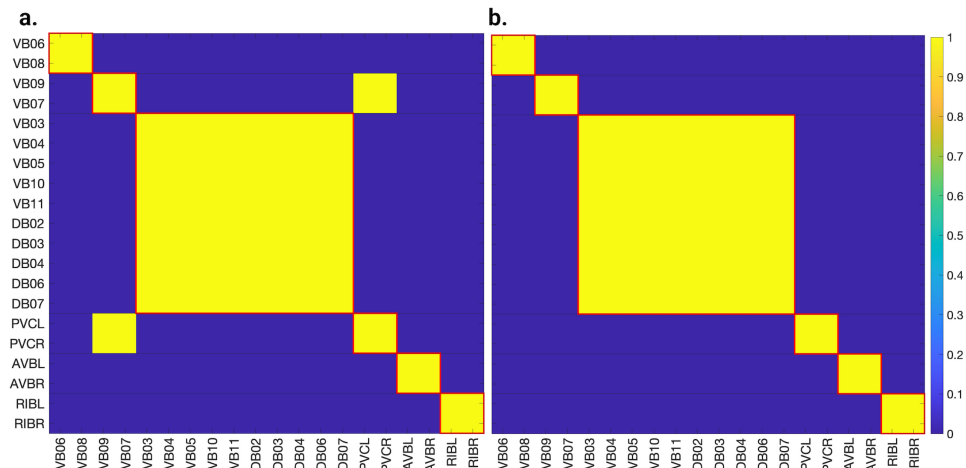


Fig 13. Forward chemical type II model simulations with no external stimuli. Synaptic variables initially centered around s_{eq} with a standard deviation of 0.1 and initial voltages set to a mean of $-35mV$ with a $10mV$ standard deviation. a) The left portion pertains to the network with binary edges and b) the right portion is associated to the integer weight case. The block system shows the result of the *LoS* measurement done on the last second of the simulations. The right *LoS* matrix is an example of an ideal case. The red-lined boxes are visual indicators for the cluster synchronization of neurons under their expected balanced coloring partitioning.

In Fig 14 it can be observed how these neurons belonging to different fibers become synchronous. Curiously one can notice that PVC neurons synchronize with each other and so do neuron VB07 and VB09 with each other before these two fibers synchronize.

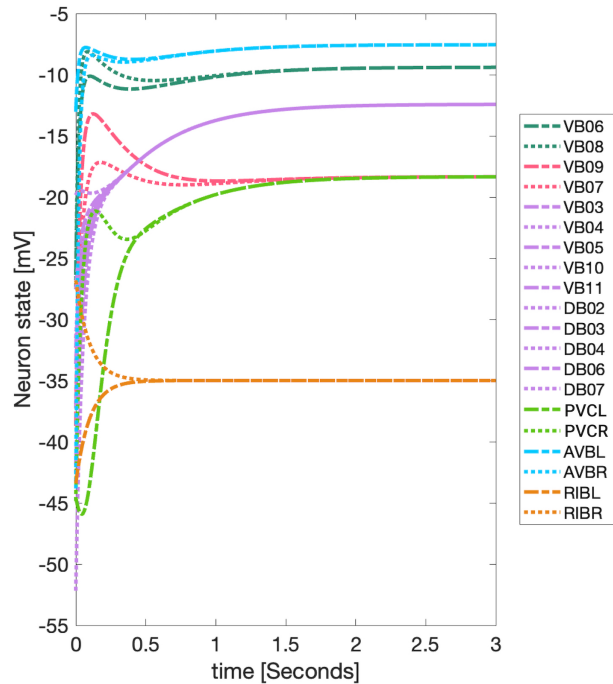


Fig 14. Binary forward chemical type II model simulations with no external stimuli. Synaptic variables initially centered around s_{eq} with a standard deviation of 0.1 and initial voltages set to a mean of $-35mV$ with a $10mV$ standard deviation. Lines are color coded based on their fiber partitioning where it can be seen that all same colored neurons eventually synchronize with each other. Neurons PVC belonging to one fiber become synchronous before synchronizing with neurons VA08 and VA09 belonging to another fiber. The LoS associated with this simulation can be observed in Fig 13a where the latter example is captured by the only off diagonal blocks.

Simulation test 2

In this section, we aim to investigate the predictive power of fiber and orbit partitionings by simulating neural activity. To achieve this, we drive the four networks by delivering the same stimulus through left-right inter-neuron pairs. These left-right inter-neuron pairs belong to the same partition in all four networks, therefore not break the fiber partitioning.

However, it is important to ensure that the external stimuli do not induce any instabilities that could complicate the interpretation of results. Therefore, we conduct a stability analysis of the ODEs to determine the range within which the external stimuli does not cause any instabilities. As a common practice in the study of dynamical systems, we focus on the Jacobian of the model under study. For the Gap junction it's Jacobian can be written as:

$$\mathbf{J}_{Gap} = -\alpha^{leak}\mathbf{I} - \alpha^{gap}\mathbf{L} \quad (22)$$

where \mathbf{I} is the identity matrix and \mathbf{L} is the Laplacian of the gap junction adjacency matrix. Notice that Eq (22) is independent of any external stimuli. The Jacobian matrix is a useful tool for investigating the stability of a system's equilibrium point. By analyzing the eigenvalues of the Jacobian matrix, we can gain insight into the local behavior of the system near it's equilibrium point. As a rule of thumb, if all eigenvalues are real and negative, then the system is stable, meaning that any small perturbations

from the equilibrium point will dampen over time, and the system will return to its steady state. If one or more eigenvalues have positive real parts, then the system is unstable, and any small perturbations will cause the system to diverge from the equilibrium point [93,94].

We find that all eigenvalues of Eq (22) are negative for the values of α^{leak} and α^{gap} as described in the ODE parameters and implementation methods section. Therefore the gap junction model is stable under any external stimuli as it does not depend on I^{ext} .

Moving on, the individual terms of the Jacobian for the Chem type I model takes the form of Eq (23). At equilibrium, the sigmoid functions have a value of 0.5 (as per how $V^{threshold}$ is constructed in this model [82]). The Jacobian for this chemical model depends on the external stimuli indirectly through V_i (Eq (19)) situated in the off-diagonal terms of the Jacobian.

$$\mathbf{J}_{ChemI} : \frac{\partial V_i}{\partial V_j} = -\alpha^{leak} \delta_{ij} - \alpha^{chem} \delta_{ij} \sum_{j=1}^n \tilde{A}_{ji}^{chem} \Phi(V_j) + \alpha^{chem} \tilde{A}_{ji}^{chem} \Phi(V_j) (1 - \Phi(V_j)) \gamma (V_i - V_{s,j}) (1 - \delta_{ij}) \quad (23)$$

Analyzing the eigenvalues of the Jacobian matrix at the stable point solutions when $V_i = V_i^{threshold}$, determined by Eq (17), shows which neurons will have unstable voltages for a given I_j^{ext} . For the F-Chem network with integer weights under the Chem type I model, most of these eigenvalues remain real and negative as the external stimuli applied to neurons PVC or AVB are varied from $-500pA$ to $500pA$. An exception occurs for the eigenvectors associated with the neurons that receive external stimuli. For PVC stimulation, an eigenvalue linearly crosses into the positive real regime for external stimuli greater than $3.08pA$ or less than $-2.38pA$ (Fig 15a). This eigenvalue is accompanied by another that mirrors its behavior. These two eigenvalues have the same value at $0.35pA$ of external stimuli (dashed black line in Fig 15). This occurs because when the external stimuli take this value, the leaking potential term in Eq (11) and Eq (12) approaches zero. Simulations of this model for the respective network show a bifurcation between the left and right PVC inter-neurons values at values higher than $3.08pA$ of external stimuli. A similar result can be observed for the stimulating neurons AVA in the backward chemical network with binary weights as seen in Fig 15b. No simulation with negative external stimuli produced bifurcations.

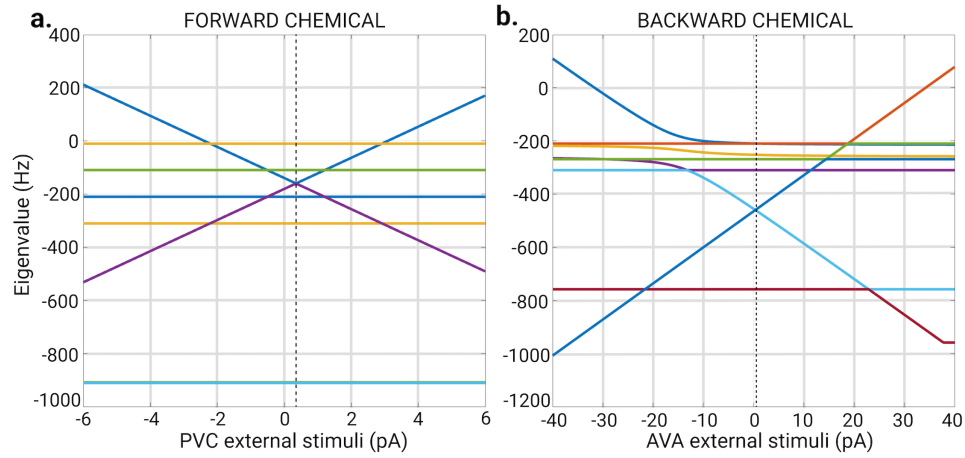


Fig 15. Stability analysis results. (Left) Eigenvalues of the Jacobian for the integer edge weighted F-Chem network under the Chem type I model as the external stimuli through inter-neurons PVC is incremented from $-6pA$ to $6pA$. The first positive eigenvalue happens at $3.08pA$ of external stimuli. (Right) Eigenvalues of the Jacobian for the integer edge weighted B-Chem network under the Chem type I model as a function of constant external stimuli input through AVA inter-neurons. First positive eigenvalue happens at $34.1pA$ of external stimuli.

A look into the Jacobian of the Chem type II model Eq (24) also indicates that it is stable under external stimuli which do not exceed specific values. Below one can find its Jacobian.

$$\mathbf{J}_{ChemII} = \begin{bmatrix} \frac{\partial \mathbf{V}}{\partial V} & \frac{\partial \mathbf{V}}{\partial s} \\ \frac{\partial \mathbf{S}}{\partial V} & \frac{\partial \mathbf{S}}{\partial s} \end{bmatrix}, \mathbf{V} = \{\dot{V}_i\}, \mathbf{S} = \{\dot{s}_i\}. \quad (24)$$

At equilibrium, the voltage values of the neurons equal that of the $V^{threshold}$ as in Eq (17) [82]. Therefore, the sigmoid function takes a value of 0.5, and the synaptic variable term equals s_{eq} . This Jacobian is indirectly affected by the external stimuli through the V_i terms, which only appear in the off-diagonal term $\frac{\partial \mathbf{V}}{\partial s}$ as it can be seen in Eq (25).

$$\frac{\partial \mathbf{V}_i}{\partial s_j} = -\alpha^{chem} \tilde{A}_{ji}^{chem} V_i (1 - \delta_{ij}) \quad (25)$$

This and other stability analysis were carried out for all the combinations of ODE models, networks, and edge types with external stimuli varying from $0pA$ to $500pA$. In Table 1, we show the results where the values of this table indicate the strength of the external stimuli (into the respective inter-neuron pairs indicated) at which the first positive eigenvalue appeared. For all cases, only one positive eigenvalue (value underscored in Table 1) was above a reasonable strength based on multiple electrophysiological studies done on *C. elegans* [43, 44, 95].

ODE MODEL	NETWORK	NEURONS	BINARY(pA)	INTEGER(pA)
CHEM TYPE I	Forward	PVC	1.5	3.08
		AVB	14.46	<u>265.4</u>
	Backward	AVA	54.15	34.1
		AIB+RIM	2.29	2.29
		AVD	11.31	14.83
CHEM TYPE II	Forward	PVC	1.06	1.25
		AVB	58.72	4.51
	Backward	AVA	13.6	8.51
		AIB+RIM	1.12	1.12
		AVD	4.89	3.46

Table 1. Instability analysis. Results for all combinations of chemical ODE models, networks and edge types. An external stimuli drove each of these networks through increasing strength from 0 up to 500pA until a positive eigenvalue emerged. These neurons are shown in the third column. Results are given in pico-Amperes.

Knowing the maximum strength of the external stimuli at which no instabilities appear, we stimulate their respective network + ODE model with a constant input equal to 90% of the external stimuli necessary to cause instability in the network plus a sinusoidal (or noise) stimulus with an amplitude 5% of the instability strength. To test through simulations that the neurons of these graphs synchronize to those stipulated by Fiber and/or Orbit partitioning we stimulate some of the neuron in these network. For the Gap junction networks were driven the dynamics of this network through inter-neurons AVB and motor-neuron DB04 for the forward network and inter-neurons AVA and motor-neuron DA05 for the backward network. This additional driving signal applied to a motorneuron is needed for the Gap junction models as these networks globally synchronize if there is only one driving signal irrespective of the network. The introduction of a second signal with different characteristics (frequency and phase) aids in breaking the global synchronization revealing the expected cluster synchronizations. For the Chemical synapses networks we stimulate PVC neurons for the forward network and neruons AVA for the backward network. We set the inter-neurons frequency to 2Hz and that of the motor neurons to 1Hz. We calculated the *LoS* matrix for each of these simulations and rounded entries lower than 1 to 0.

These resulting matrices were subtracted from their idealized *LoS* matrix obtained from fiber partitioning where these have diagonal block elements equal 1 (for each fiber) and all other entries equal zero (delineated with red lines in Fig 11, Fig12 and Fig 13). This subtraction was divided by 2 times the number of elements in *LoS* matrix without counting diagonal elements. A zero value in these indicates a perfect agreement with the idealized *LoS* matrix from fiber partitioning. A negative value indicates additional synchronization between two or more balanced colored groups. A positive value would indicate that the expected fiber partitionings were not found or disagree in some form.

Table 2 presents the results of our analysis. According to these results, all networks, regardless of the ODE model or type of edge, separate into distinct synchronous groups under the *LoS* metric. This finding confirms the partitions obtained via fiber partitioning. We did not observe any agreement in orbit coloring for the B-Chem network, which would have led to a positive entry in Table 2 by dividing diagonal boxes into two or more diagonal boxes. The negative values in this table indicate that some of the cluster cells expected from fiber partitioning synchronize with one another, but this is not a negative result because fiber partitioning only requires neurons in a fiber to synchronize and does not preclude different fibers from synchronizing.

ODE MODEL	NETWORK	BINARY	INTEGER
CHEM TYPE I	Forward	0	0
	Backward	-0.009	0
CHEM TYPE II	Forward	0	0
	Backward	0	0
GAP TYPE	Forward	-0.12	0
	Backward	-0.16	-0.16

Table 2. Synchronization among Fibers. Synchronization difference between the *LoS* matrix of a driven network and its ideal *LoS* matrix. A value of zero indicates perfect agreement between the *LoS* matrix of a driven networks and its ideal *LoS* matrix with distinct synchronous groups. A negative value indicates that two or more minimal balanced colorings have the same value at the same time. A positive value would indicate that the dynamics of its neurons do not cluster synchronize to the partitioning of the minimal balanced coloring. The networks here were driven through inter-neurons mentioned in Sections . The best ODE model to differentiate synchronous partitionings was the Chem type II model.

Simulation test 3

We examined neuron synchronization and fiber partitioning agreement, testing robustness by adding/subtracting random edge weights to simulate missing or incorrect information. We added normal distribution noise (std. dev. 0-0.1 in 0.01 steps) to all weights, and drove the same neurons as in **simulation test 2** ten times with all these resulting *LoS* being averaged (see *LoS* matrices of Fig 16). The *LoS* obtained from **simulation test 2** was binarized (elements below a value of 1 were zeroed as well as elements in the diagonal) and used as a mask on the averaged results. The resulting matrices were subtracted from the masking matrix.

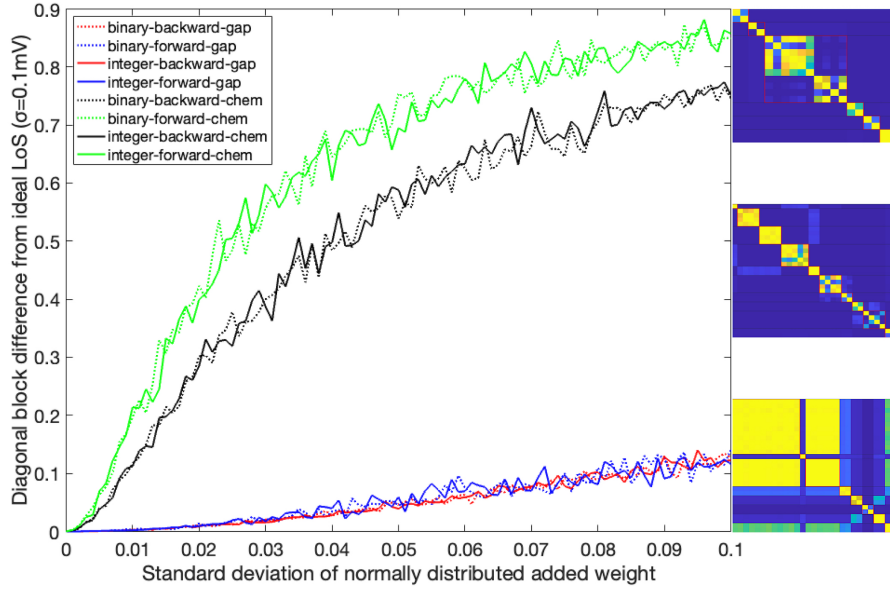


Fig 16. Effects on synchronicity due to randomizing non-zero weights. The addition of a normally distributed amount (with zero mean) to the non-zero weights of all the networks studied here (Gap and Chem type II models) is studied. Each perturbed network is simulated for 5 seconds with the last second used to calculate its *LoS* and subtracted from the idealized *LoS* (see Fig 13b for an example). The difference is only calculated on the expected minimal balanced coloring synchronizations (diagonal blocks). Examples of the *LoS* calculated for the F-Chem-Integer, B-Chem-Integer and B-Gap-Integer networks are shown from top to bottom respectively.

In this simulation, the driving signals are composed of a constant input of $0.1pA$ and an oscillatory term with a frequency of $2Hz$ for inter-neurons and $1Hz$ for motor-neurons. The amplitude was set to $0.5pA$ and a Gaussian random walk scaled between $-0.01pA$ and $0.01pA$. All initial voltages were set to $-35mV$, and all initial synaptic variables to s_{eq} . Fig 16 shows the results. Varying weights affects *LoS* synchronicity of networks similarly, regardless of binary or integer edge weights (continuous and dotted lines, respectively). Backward chemical locomotion network is slightly more robust to weight changes than forward chemical locomotion network. All gap junction model synchronizations are robust to weight changes. However, most synchronicities were lost when measured through the strict *LoS* method, which requires signals to have the same value at the same time within a distance less than $\sigma = 0.1mV$. Different synchronicity measures may lead to different conclusions about the dynamics of stimulated networks. For instance, in the case of the integer edge-weighted F-Chem network with edge weights having a standard deviation of 0.5, its dynamics are illustrated in Fig 17. Although *LoS* analysis shows no synchronizations, the *PLV* metric demonstrates that neurons of the same minimal balanced coloring exhibit high synchronicity under phase synchronicity. As such, by relaxing the constraint of synchronicity from having the same value simultaneously to having the same instantaneous phase, it is possible to highlight the synchronicities expected from fibration symmetries. This was seen for all other networks as well.

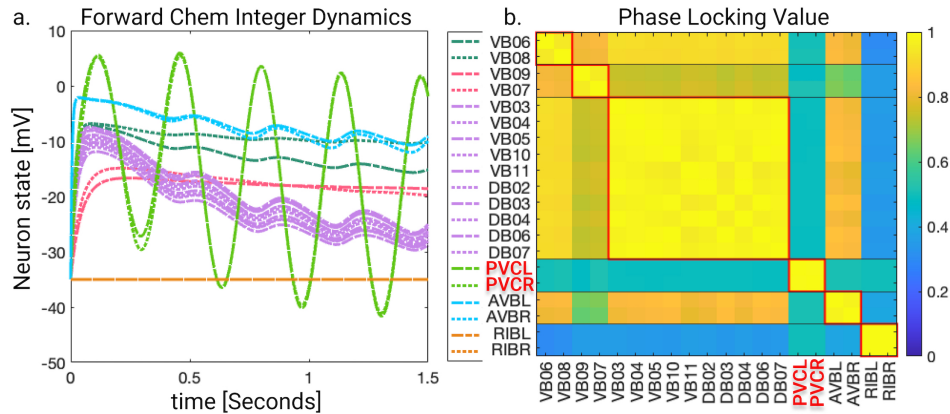


Fig 17. Phase synchronization results. (a) Dynamics for the forward chemical integer edge weighted network (with an average edge weight of 2.6 before any edge alterations). This network was driven through inter-neurons PVC as explained in section: Simulation test 3. The alterations to its edges weights were done by adding to them normally distributed numbers with standard deviation 0.5 and mean 0. (b) Phase Locking Value (*PLV*) matrix of these dynamics.

Discussion

We found that, in the case of the gap junction networks presented here, orbits and fibers coincide. This is a direct consequence of an undirected graph, where nodes have the same value for their in/out-degree. This similarity is lost when considering a directed graph where this condition is broken. Generally, in a directed graph, orbits and fibers do not coincide (unless some modular structures are present). As expected, we found that in these circumstances, the number of fibrations symmetries was higher than the automorphism symmetries (due to the less restrictive constraints) for only one of the networks. More symmetries translate to less number of clusters, as depicted in Fig 7.

We discovered a non-trivial fiber partitioning of various neuronal classes. Across all subnetworks studied, we found that the left- and right members of each interneurons class AVA, AVE, AVD, AVB and RIB each receive a class-specific balanced coloring (Figures 5-7). This is consistent with our previous findings that pairwise correlations between the activities of left- right- bilaterally symmetric neurons are the strongest across the worm brain [17]. Moreover, we find that motoneurons in the ventral cord partition into unexpected sub-groups, that are not simply explained by their body positions along the anterior- to posterior body axis, nor by the body wall muscle segments they innervate (Figures 5-7). These motoneurons have yet not been recorded and identified altogether simultaneously, however our previous work indicates that all A-class and all B-class motor neurons are highly correlated with each other respectively when recorded in immobilised worms (reference. Kaplan, Salazar 2021). Our analyses performed here suggests, that those subgroups that receive the same balanced coloring synchronise further, a prediction that can be tested in future whole nervous system calcium imaging recordings. We speculate that these subgroups also relate to each other functionally, by perhaps contributing similarly to the worms locomotion behavior or controlling different aspects of it e.g. undulation speed, curvature or other aspects of body posture. Testing this hypothesis will require recording their activity simultaneously in freely crawling worms.

The fiber building blocks (FBB) of the directed networks with binary edges were explored. It was discovered that the B-Chem network is conformed by Fibonacci fibers

which indicates that the interneurons conforming this network have nested loops which indicate a high degree of complexity for this group of nodes driving the motor-neurons of the system. For the F-Chem network did not show to be conformed by the FBB with nested loops but did show that some of its motor-neurons are composed by multilayered building blocks indicating that some of the neurons of this system become synchronous indirectly through neurons with two degrees of separation. This helps with the robustness of the network as destroying some neurons will not affect the synchronicity of other neurons in the same fiber. Our partitioning into elementary building blocks suggest that some of these motifs serve some computational roles in the generation of locomotion. Whole nervous system calcium imaging recording of all of these neurons simultaneously could provide insights into the types of these computations.

Understanding the stability of the equations used to simulate the neuronal interactions in these networks aided to determine the parameter space for which the partitions under different conditions were valid. The equitable partitions found by fibration and automorphism theory predicts only the existence of the cluster synchronization solutions and does not mention anything about their stability. Investigation of this aspect can only be done numerically. We performed simulations of interacting simulations according to Eq (9).

First, we assume no external stimuli, and we compare the partitions found by means of fibrations in the *C. elegans* network with those found through the Level of Synchronicity measure (*LoS*) based on dynamical simulations. For all networks and for all admissible ODE models regardless of the edge type we found perfect agreement between the expected minimal balanced coloring partitionings and the block of synchronicity. For the F-Chem type II weighted case, we found perfect separation of the expected fibers. In the binary case, we find that inter-neurons PVC and motor-neurons VB07 and VB09 synchronize. This deviation is more evident in the case of B-chem networks, where several minimally balanced colorings became synchronous with other minimal balanced colorings. Having two or more distinct clusters (a group of neurons with the same balance coloring) be synchronous with each other is not an unexpected result and can be expected based on the theory of equitable graph partitionings such as that of orbits and fibers. While the theory does stipulate that two nodes with the same balanced coloring will be synchronous, it does not stipulate that two nodes with different balanced coloring will not be synchronous. There are no restrictions to how differently colored nodes behave [27, 96].

Overall, the integer-weighted version of the Chem network with synaptic variables is the best model when it comes to distinctively separating expected synchronous groups regardless of the ODE model. The final synchronization remained the same as in Fig 12 as the standard deviations for the initial voltages and synaptic variables varied from 0 to 0.1. This configuration is expected as the stable point solutions ($V^{threshold}$) of any of these models are independent of initial conditions [51, 82].

To simulate more realistic conditions, we increased the external stimuli, ensuring not to change the partitionings of the networks (balanced colored external stimuli). We found that the gap junction model is stable under any external stimuli as it does not depend on the external factor I^{ext} .

As for Chem networks, we found that at a strength greater than the ones indicated in Table 1, a voltage bifurcation arose for the pair of neurons with a I^{ext} greater than zero and, by such, broke the pair's predicted synchronization from that of the minimal balanced coloring. The expected synchronization patterns of all other neurons remained the same as the ones predicted by the minimal equitable partitioning. All but one (underlined value) of the values in Table 1 seem within reasonably stable. This is consistent with electrophysiological recordings of a set of *C. elegans* neurons showing stable responses when stimulated with an external current source [14, 43, 95].

We found that integer-weighted chemical networks are more resistant to external stimuli when it comes to preserving their fiber structure. Their binary version behaves similarly, but for the case of B-chem, type II. No orbit coloring agreement was found for the B-Chem network. An agreement of this type would have led to a positive value in Table 2, a result due to diagonal boxes being divided into two or more diagonal boxes (because we already know there are more orbits than fibers in this case, as noticed in the previous section).

We finally repeated the previous analyses in the scenario where only partial information about the connectome networks is available. According to our findings, missing information affects in a similar way both the binary and weighted versions of a given network. Nevertheless, gap-junctions networks are more robust to missing information, followed by backward chemical networks. Nevertheless, almost all synchronicities were lost when measured through the *LoS* method. This is due to the strong constraints required by the *LoS* metric. Indeed different metrics, like the *PLV*, reveal that neurons of the same minimal balanced coloring are still highly synchronous under phase synchronicity. These findings are also in par with [66] where a simple symmetric network of artificial neurons constructed from resistors and capacitors is still able to achieve synchronization for most configurations even though these components have an approximate 5% error in their expected parameters. The change in the networks weight can be transformed into each neuron having a different coupling strength (σ^{Chem} or σ^{Gap}) where the networks weight are returned to their integer or binary setting.

The end goal of studying these sub-networks is to predict synchronization based on the connectivity patterns which based on theory these should be reflected as activity patterns in live recordings [17]. Indeed, Haspel *et al.* [97] created a repeating unit containing the different classes of motor-neurons and body-wall muscles that intend to capture missing links from [8]. Six of these units are stitched together in series to form the entirety of a symmetric neural infrastructure underlying the locomotion of the *C. elegans*; this inherently leads to the synchronicity of the neurons and muscles when modeled through simulations [98]. Similarly, we use symmetrized networks which are repaired versions of an original connectome that preserve most of the original structure. On the repaired networks, we measure fibration symmetries to predict the synchronization of neurons based on their structure.

Conclusion

Here, we present a theoretical framework suggesting that symmetries in the graph structure of a neuronal network underlie functional synchronizations. We explored some of the fiber building block of the networks presented here and found that they are composed by multilayered blocks or by block with nested loops. It was also shown that minimal balanced coloring could be successfully used to determine the synchronicity patterns of all the symmetrized networks. Its performance is best when only synaptic interactions are present compared to when only gap junction interactions are present mainly because zero to few different fiber become synchronous. Fiber and orbit symmetries were able to capture the synchronicity patterns that appear in purely gap junction networks. However, these synchronicity patterns are subtly distinguishable. All the undirected networks analyzed in this paper became globally synchronized when driven by constant input. Only when these gap junction networks were driven by sinusoidal and random stimuli did most of the predicted synchronicity groups recover. The simulation results hold true when compared to fiber coloring and should be a go to tool when creating symmetric networks for the *C. elegans* where simulation may be skipped as could have been the case in [59,98].

On the contrary, orbit colorings do not perform as well as balance coloring in predicting synchronizations in ODEs models like Eq (9). If the system of coupled ODEs used accounted for the number of out going edges by varying some parameter, the dynamics of the neurons would possibly partition into the cluster predicted by orbit colorings. However, as of now, neurons and their potentials are known to only be affected by their inputs and not by the number of their synaptic outputs, therefore its reasonable to expect that the synchronizations of neurons in a connectome will obey fiber symmetries over orbit symmetries.

This study was performed under a set of idealised prerequisites i.e., a repaired connectome, nodes and edges with identical biophysical properties and isolated chemical- and gap junction networks. We, however, suggest that the network features described here significantly contribute to the activity patterns observable in the biological neuronal network of *C. elegans*. Our work makes testable predictions about neuronal ensembles that are expected to show elevated synchronicity and might group functionally in their control of locomotion. In future studies, we will test these predictions using experimental neuronal recording and circuit interrogation techniques. In the future, our approach can be applied to larger connectome datasets i.e., those of larval or adult fruit flies [6, 99].

Acknowledgments

Thanks to Wolfram Liebermeister for his suggestion to explore the effects of altering the weights of these networks. And thanks to Paolo Boldi for clearing out the air when it came to some equitable partitioning concepts.

Author Contributions

Author contributed in the following manners. Hernan Makse: Conceptualization, Funding Acquisition, Writing – Original Draft Preparation. Manuel Zimmer: Conceptualization, Funding Acquisition, Writing – Review & Editing. Matteo Serafino: Project Administration. Pedro Augusto: Validation. Bryant Avila: Investigation, Methodology, Software, Validation, Visualization, Writing – Original Draft Preparation, Writing – Review & Editing.

Funding

Funding leading to the results of this work was provided by NIBIB and NIMH through the NIH BRAIN Initiative Grant # R01 EB028157. M.Z. is supported by the Simons Foundation (#543069). The IMP is funded by Boehringer Ingelheim.

Data and code

GitHub repository containing a user friendly Matlab app capable of reproducing any of the simulation carried out in this paper and having additional tools not mentioned here can be found at: https://github.com/maskelab/Celegans_foward_and_backward_symmetric_dynamics

References

1. White JG, Southgate E, Thomson JN, Brenner S, et al. The structure of the nervous system of the nematode *Caenorhabditis elegans*. *Philos Trans R Soc Lond B Biol Sci*. 1986;314(1165):1–340.
2. Ryan K, Lu Z, Meinertzhagen IA. The CNS connectome of a tadpole larva of *Ciona intestinalis* (L.) highlights sidedness in the brain of a chordate sibling. *Elife*. 2016;5:e16962.
3. Eichler K, Li F, Litwin-Kumar A, Park Y, Andrade I, Schneider-Mizell CM, et al. The complete connectome of a learning and memory centre in an insect brain. *Nature*. 2017;548(7666):175–182.
4. Veraszto C, Jasek S, Gühmann M, Shahidi R, Ueda N, Beard JD, et al. Whole-animal connectome and cell-type complement of the three-segmented *Platynereis dumerilii* larva. *BioRxiv*. 2020; p. 2020–08.
5. Abbott LF, Bock DD, Callaway EM, Denk W, Dulac C, Fairhall AL, et al. The mind of a mouse. *Cell*. 2020;182(6):1372–1376.
6. Winding M, Pedigo BD, Barnes CL, Patsolic HG, Park Y, Kazimiers T, et al. The connectome of an insect brain. *Science*. 2023;379(6636):eadd9330.
7. Curto C, Morrison K. Relating network connectivity to dynamics: opportunities and challenges for theoretical neuroscience. *Current opinion in neurobiology*. 2019;58:11–20.
8. Varshney LR, Chen BL, Paniagua E, Hall DH, Chklovskii DB. Structural properties of the *Caenorhabditis elegans* neuronal network. *PLoS computational biology*. 2011;7(2):e1001066.
9. Cook SJ, Jarrell TA, Brittin CA, Wang Y, Bloniarz AE, Yakovlev MA, et al. Whole-animal connectomes of both *Caenorhabditis elegans* sexes. *Nature*. 2019;571(7763):63–71.
10. Witvliet D, Mulcahy B, Mitchell JK, Meirovitch Y, Berger DR, Wu Y, et al. Connectomes across development reveal principles of brain maturation. *Nature*. 2021;596(7871):257–261.
11. Qian J, Hintze A, Adami C. Colored motifs reveal computational building blocks in the *C. elegans* brain. *PLoS One*. 2011;6(3):e17013.
12. Watts DJ, Strogatz SH. Collective dynamics of ‘small-world’ networks. *nature*. 1998;393(6684):440–442.
13. Towlson EK, Vértes PE, Yan G, Chew YL, Walker DS, Schafer WR, et al. *Caenorhabditis elegans* and the network control framework—FAQs. *Philosophical Transactions of the Royal Society B: Biological Sciences*. 2018;373(1758):20170372.
14. Sohn Y, Choi MK, Ahn YY, Lee J, Jeong J. Topological cluster analysis reveals the systemic organization of the *Caenorhabditis elegans* connectome. *PLoS computational biology*. 2011;7(5):e1001139.
15. Jarrell TA, Wang Y, Bloniarz AE, Brittin CA, Xu M, Thomson JN, et al. The connectome of a decision-making neural network. *science*. 2012;337(6093):437–444.

16. Brittin CA, Cook SJ, Hall DH, Emmons SW, Cohen N. A multi-scale brain map derived from whole-brain volumetric reconstructions. *Nature*. 2021;591(7848):105–110.
17. Uzel K, Kato S, Zimmer M. A set of hub neurons and non-local connectivity features support global brain dynamics in *C. elegans*. *Current Biology*. in press. 2022;.
18. Maertens T, Schöll E, Ruiz J, Hövel P. Multilayer network analysis of *C. elegans*: Looking into the locomotory circuitry. *Neurocomputing*. 2021;427:238–261.
19. Tsuyuzaki K, Yamamoto K, Toyoshima Y, Sato H, Kanamori M, Teramoro T, et al. WormTensor: a clustering method for time-series whole-brain activity data from *C. elegans*. 2022;.
20. Nathe C, Gambuzza LV, Frasca M, Sorrentino F. Looking beyond community structure leads to the discovery of dynamical communities in weighted networks. *Scientific reports*. 2022;12(1):1–12.
21. Schaub MT, O’Clery N, Billeh YN, Delvenne JC, Lambiotte R, Barahona M. Graph partitions and cluster synchronization in networks of oscillators. *Chaos: An Interdisciplinary Journal of Nonlinear Science*. 2016;26(9):094821.
22. Leifer I, Sánchez-Pérez M, Ishida C, Makse HA. Predicting synchronized gene coexpression patterns from fibration symmetries in gene regulatory networks in bacteria. *BMC bioinformatics*. 2021;22:1–34.
23. Stewart I, Golubitsky M, Pivato M. Symmetry groupoids and patterns of synchrony in coupled cell networks. *SIAM Journal on Applied Dynamical Systems*. 2003;2(4):609–646.
24. Antoneli F, Stewart I. Symmetry and synchrony in coupled cell networks 2: Group networks. *International Journal of Bifurcation and Chaos*. 2007;17(03):935–951.
25. Sorrentino F, Pecora LM, Hagerstrom AM, Murphy TE, Roy R. Complete characterization of the stability of cluster synchronization in complex dynamical networks. *Science advances*. 2016;2(4):e1501737.
26. Morone F, Leifer I, Makse HA. Fibration symmetries uncover the building blocks of biological networks. *Proceedings of the National Academy of Sciences*. 2020;117(15):8306–8314.
27. Boldi P, Vigna S. Computing anonymously with arbitrary knowledge. In: *Proceedings of the eighteenth annual ACM symposium on Principles of distributed computing*; 1999. p. 181–188.
28. Boldi P, Vigna S. Fibrations of graphs. *Discrete Mathematics*. 2002;243(1-3):21–66.
29. Gambuzza LV, Frasca M. A criterion for stability of cluster synchronization in networks with external equitable partitions. *Automatica*. 2019;100:212–218.
30. Aguiar MA, Dias APS. Synchronization and equitable partitions in weighted networks. *Chaos: An Interdisciplinary Journal of Nonlinear Science*. 2018;28(7):073105.

31. Golubitsky M, Stewart I. Nonlinear dynamics of networks: the groupoid formalism. *Bulletin of the american mathematical society*. 2006;43(3):305–364.
32. Kudose S. Equitable partitions and orbit partitions. *Acta Mathematica Sinica*. 2009; p. 1–9.
33. Stewart I. Balanced Colorings and Bifurcations in Rivalry and Opinion Networks. *International Journal of Bifurcation and Chaos*. 2021;31(07):2130019.
34. Servatius H. Automorphisms of graph groups. *Journal of Algebra*. 1989;126(1):34–60.
35. Boldi P, Leifer I, Makse HA. Quasifibrations of graphs to find symmetries and reconstruct biological networks. *Journal of Statistical Mechanics: Theory and Experiment*. 2022;2022(11):113401.
36. Nijholt E, Rink B, Sanders J. Graph fibrations and symmetries of network dynamics. *Journal of Differential Equations*. 2016;261(9):4861–4896.
37. Morone F, Makse HA. Symmetry group factorization reveals the structure-function relation in the neural connectome of *Caenorhabditis elegans*. *Nature communications*. 2019;10(1):1–13.
38. Leifer I, Morone F, Reis SD, Andrade Jr JS, Sigman M, Makse HA. Circuits with broken fibration symmetries perform core logic computations in biological networks. *PLoS computational biology*. 2020;16(6):e1007776.
39. Milo R, Shen-Orr S, Itzkovitz S, Kashtan N, Chklovskii D, Alon U. Network motifs: simple building blocks of complex networks. *Science*. 2002;298(5594):824–827.
40. Alon U. Network motifs: theory and experimental approaches. *Nature Reviews Genetics*. 2007;8(6):450–461.
41. Alon U. Network motifs: the building blocks of complex networks. *Journal of Physiology-Paris*. 2007;101(1-3):1–6.
42. Nazerian A, Panahi S, Leifer I, Phillips D, Makse HA, Sorrentino F. Matryoshka and disjoint cluster synchronization of networks. *Chaos: An Interdisciplinary Journal of Nonlinear Science*. 2022;32(4):041101.
43. Faumont S, Boulin T, Hobert O, Lockery SR. Developmental regulation of whole cell capacitance and membrane current in identified interneurons in *C. elegans*. *Journal of neurophysiology*. 2006;95(6):3665–3673.
44. Lindsay TH, Thiele TR, Lockery SR. Optogenetic analysis of synaptic transmission in the central nervous system of the nematode *Caenorhabditis elegans*. *Nature communications*. 2011;2(1):306.
45. Husson SJ, Gottschalk A, Leifer AM. Optogenetic manipulation of neural activity in *C. elegans*: from synapse to circuits and behaviour. *Biology of the Cell*. 2013;105(6):235–250.
46. Kobayashi J, Shidara H, Morisawa Y, Kawakami M, Tanahashi Y, Hotta K, et al. A method for selective ablation of neurons in *C. elegans* using the phototoxic fluorescent protein, KillerRed. *Neuroscience letters*. 2013;548:261–264.
47. Taylor SR, Santpere G, Weinreb A, Barrett A, Reilly MB, Xu C, et al. Molecular topography of an entire nervous system. *Cell*. 2021;184(16):4329–4347.

48. Altun Z, Hall D, Herndon L, Wolkow C, Crocker C. WormAtlas;. <http://www.wormatlas.org>.
49. Leifer I, Phillips D, Sorrentino F, Makse HA. Symmetry-driven network reconstruction through pseudobalanced coloring optimization. *Journal of Statistical Mechanics: Theory and Experiment*. 2022;2022(7):073403.
50. Chalfie M, Sulston JE, White JG, Southgate E, Thomson JN, Brenner S. The neural circuit for touch sensitivity in *Caenorhabditis elegans*. *Journal of Neuroscience*. 1985;5(4):956–964.
51. Wicks SR, Roehrig CJ, Rankin CH. A dynamic network simulation of the nematode tap withdrawal circuit: predictions concerning synaptic function using behavioral criteria. *Journal of Neuroscience*. 1996;16(12):4017–4031.
52. Driscoll M, Kaplan J. Mechanotransduction. In “*C. elegans II*” (TBDA Riddle, BJ Meyer, and JR Priess, Eds.); 1997.
53. M C, G WJ. “The nervous system” in *The nematode Caenorhabditis elegans*. 1988; p. 337–392.
54. Tolstenkov O, Van der Auwera P, Costa WS, Bazhanova O, Gemeinhardt TM, Bergs AC, et al. Functionally asymmetric motor neurons contribute to coordinating locomotion of *Caenorhabditis elegans*. *Elife*. 2018;7.
55. Deng L, Denham JE, Arya C, Yuval O, Cohen N, Haspel G. Inhibition underlies fast undulatory locomotion in *Caenorhabditis elegans*. *Eneuro*. 2021;8(2).
56. Hammond C. *Cellular and molecular neurophysiology*. Academic Press; 2014.
57. Palacios-Prado N, Huetteroth W, Pereda AE. Hemichannel composition and electrical synaptic transmission: molecular diversity and its implications for electrical rectification. *Frontiers in cellular neuroscience*. 2014;8:324.
58. Marder E. Electrical synapses: rectification demystified. *Current Biology*. 2009;19(1):R34–R35.
59. Haspel G, O’Donovan MJ, Hart AC. Motoneurons dedicated to either forward or backward locomotion in the nematode *Caenorhabditis elegans*. *Journal of Neuroscience*. 2010;30(33):11151–11156.
60. Kato S, Kaplan HS, Schrödel T, Skora S, Lindsay TH, Yemini E, et al. Global brain dynamics embed the motor command sequence of *Caenorhabditis elegans*. *Cell*. 2015;163(3):656–669.
61. Kaplan HS, Thula OS, Khoss N, Zimmer M. Nested neuronal dynamics orchestrate a behavioral hierarchy across timescales. *Neuron*. 2020;105(3):562–576.
62. Siddique AB, Pecora L, Hart JD, Sorrentino F. Symmetry-and input-cluster synchronization in networks. *Physical Review E*. 2018;97(4):042217.
63. Kalloniatas AC, Zuparic ML. Fixed points and stability in the two-network frustrated Kuramoto model. *Physica A: Statistical Mechanics and its Applications*. 2016;447:21–35.
64. Aldis JW. A polynomial time algorithm to determine maximal balanced equivalence relations. *International Journal of Bifurcation and Chaos*. 2008;18(02):407–427.

65. Dahms T, Lehnert J, Schöll E. Cluster and group synchronization in delay-coupled networks. *Physical Review E*. 2012;86(1):016202.
66. Cao B, Wang YF, Wang L, Yu YZ, Wang XG. Cluster synchronization in complex network of coupled chaotic circuits: an experimental study. *Frontiers of Physics*. 2018;13:1–11.
67. Kamei H, Cock PJ. Computation of balanced equivalence relations and their lattice for a coupled cell network. *SIAM Journal on Applied Dynamical Systems*. 2013;12(1):352–382.
68. Hochschild G. The automorphism group of Lie group. *Transactions of the American Mathematical Society*. 1952;72(2):209–216.
69. Godsil CD. Compact graphs and equitable partitions. *Linear Algebra and its Applications*. 1997;255(1-3):259–266.
70. Monteiro HS, Leifer I, Reis SD, Andrade Jr JS, Makse HA. Fast algorithm to identify minimal patterns of synchrony through fibration symmetries in large directed networks. *Chaos: An Interdisciplinary Journal of Nonlinear Science*. 2022;32(3):033120.
71. DeVille L, Lerman E. Modular dynamical systems on networks. *Journal of the European Mathematical Society*. 2015;17(12):2977–3013.
72. The Sage Developers. SageMath, the Sage Mathematics Software System (Version 9.3); 2021.
73. McKay BD, Piperno A. Practical graph isomorphism, II. *Journal of symbolic computation*. 2014;60:94–112.
74. Jones GA, Jones JM. *Elementary number theory*. Springer Science & Business Media; 1998.
75. Dixon JD, Mortimer B. *Permutation groups*. vol. 163. Springer Science & Business Media; 1996.
76. Hartwell LH, Hopfield JJ, Leibler S, Murray AW. From molecular to modular cell biology. *Nature*. 1999;402(Suppl 6761):C47–C52.
77. Alon U. *An introduction to systems biology: design principles of biological circuits*. CRC press; 2019.
78. Buchanan M, Caldarelli G, De Los Rios P, Rao F, Vendruscolo M. *Networks in cell biology*. Cambridge University Press; 2010.
79. Rakowski F, Srinivasan J, Sternberg PW, Karbowski J. Synaptic polarity of the interneuron circuit controlling *C. elegans* locomotion. *Frontiers in computational neuroscience*. 2013;7:128.
80. Ermentrout B, Terman DH. *Mathematical foundations of neuroscience*. vol. 35. Springer; 2010.
81. Kim J, Leahy W, Shlizerman E. Neural interactome: Interactive simulation of a neuronal system. *Frontiers in computational neuroscience*. 2019;13:8.
82. Kunert J, Shlizerman E, Kutz JN. Low-dimensional functionality of complex network dynamics: Neurosensory integration in the *Caenorhabditis elegans* connectome. *Physical Review E*. 2014;89(5):052805.

83. Kunert-Graf JM, Shlizerman E, Walker A, Kutz JN. Multistability and long-timescale transients encoded by network structure in a model of *C. elegans* connectome dynamics. *Frontiers in computational neuroscience*. 2017;11:53.
84. Jenny M, Kathleen M RS, Noureddine M, Alicia S, Rebecca E, Alexandra B, et al. Analysis of Freely Swimming *C. elegans* Using Laser Diffraction. *Open Journal of Biophysics*. 2012;2012.
85. Koch C. *Biophysics of computation: information processing in single neurons*. Oxford university press; 2004.
86. Purves D, Augustine GJ, Fitzpatrick D, Hall W, LaMantia AS, White L. *Neurosciences*. Sunderland, MA: Sinauer Associates.; 2008.
87. Miguel MS, Toral R. Stochastic effects in physical systems. In: *Instabilities and nonequilibrium structures VI*. Springer; 2000. p. 35–127.
88. Phillips JM, Venkatasubramanian S. A gentle introduction to the kernel distance. *arXiv preprint arXiv:11031625*. 2011;.
89. Lachaux JP, Rodriguez E, Martinerie J, Varela FJ. Measuring phase synchrony in brain signals. *Human brain mapping*. 1999;8(4):194–208.
90. Godsil C, Royle GF. *Algebraic graph theory*. vol. 207. Springer Science & Business Media; 2001.
91. Chen YJ, Pan CL. An olfactory-interneuron circuit that drives stress-induced avoidance behavior in *C. elegans*. *Neuroscience Research*. 2022;.
92. Singh K, Huang H, Hart AC. Do *C. elegans* sleep? A closer look; 2013.
93. Strogatz SH. *Nonlinear dynamics and chaos: with applications to physics, biology, chemistry, and engineering*. CRC press; 2018.
94. Guckenheimer J, Holmes P. *Nonlinear oscillations, dynamical systems, and bifurcations of vector fields*. vol. 42. Springer Science & Business Media; 2013.
95. Liu Q, Kidd PB, Dobosiewicz M, Bargmann CI. *C. elegans* AWA olfactory neurons fire calcium-mediated all-or-none action potentials. *Cell*. 2018;175(1):57–70.
96. Boldi P, Vigna S. An effective characterization of computability in anonymous networks. In: *International Symposium on Distributed Computing*. Springer; 2001. p. 33–47.
97. Haspel G, O'Donovan MJ. A perimotor framework reveals functional segmentation in the motoneuronal network controlling locomotion in *Caenorhabditis elegans*. *Journal of Neuroscience*. 2011;31(41):14611–14623.
98. Olivares EO, Izquierdo EJ, Beer RD. Potential role of a ventral nerve cord central pattern generator in forward and backward locomotion in *Caenorhabditis elegans*. *Network Neuroscience*. 2018;2(3):323–343.
99. Scheffer LK, Xu CS, Januszewski M, Lu Z, Takemura Sy, Hayworth KJ, et al. A connectome and analysis of the adult *Drosophila* central brain. *Elife*. 2020;9:e57443.